Highly efficient and visible light driven $Ni_{0.5}Zn_{0.5}Fe_2O_4$@PANI modified BiOCl heterocomposite catalyst for water remediation

Ruchika Tanwar, Bikramjit Kaur, Uttam Kumar Mandal*

University School of Chemical Technology, G.G.S. Indraprastha University, Sector 16C, Dwarka, New Delhi, 110078, India

ABSTRACT

In the domain of photocatalysis the potential utilization of BiOCl is restricted in terms of efficiency and as a visible light photocatalyst due to the rapid recombination of light induced charge carriers and enduring a wide band gap. In the present work, a heterostructured $Ni_{0.5}Zn_{0.5}Fe_2O_4$@Polyaniline/BiOCl composites was prepared via a simple facile procedure to provide substantial photoinduced charge carriers separation and reduction in band gap for enhanced light harvesting in BiOCl. Visible light driven photocatalytic performance of the designed catalyst has validated by the degradation of four toxic dyes i.e., methyl orange (MO), congo red (CR), rhodamine B (Rh B), methylene blue (MB). Physiochemical and heterostructure of the synthesized photocatalyst was confirmed by PXRD, FTIR, SEM, TEM, HRTEM, XPS, EDX, PL, BET and DRS techniques. Among the various modified $Ni_{0.5}Zn_{0.5}Fe_2O_4$@Polyaniline in BiOCl the catalyst with 20 wt% $Ni_{0.5}Zn_{0.5}Fe_2O_4$@Polyaniline (NPB20) showed extended absorption edges and potential photocatalytic activity to the various dyes under visible light as compared to BiOCl. The exceptional enhancement could be scrutinized in terms of the extended light absorption by the $Ni_{0.5}Zn_{0.5}Fe_2O_4$@Polyaniline nanofibers and efficient separation of photogenerated electron-hole pairs enabling in the retardation of the photon induced charge carriers recombination. The responsible photocatalysis mechanism supported from hydroxyl radicals analysis and trapping experiments is also been explicated. Additionally, the stability and reusability study of the developed catalyst supports its broad potential applications as a visible/solar light responsive photocatalyst for water remediation.

© 2017 Elsevier B.V. All rights reserved.

1. Introduction

Around 10,000 dyes and colour pigments are used in textile industry worldwide and the effluent from these industries accounts for a major portion of the waste water [1,2]. Additionally the dyes are also widely used by other industries like food, paper, cosmetic etc and generate and accumulated coloured pollutants in water streams [3]. The coloured effluents are generally carried carcinogenic, toxic and mutagenic organic/inorganic contaminates and causes serious problems to natural water resources which effects environmental sustainability of an ecosystem [4,5]. Most of these coloured contaminants are non-biodegradable under aerobic conditions and needs their removal or degradation for remediation of aquatic environment and alleviating the damaging impact on living organisms, from plants to mammals.

TiO_2 (3.2 eV) has historically been used as a photocatalyst for the remediation of waste water due to its excellent photocatalytic activity, superior chemical stability, non-toxicity and low cost [6,7]. Unfortunately, its photocatalytic activity is restricted due to the recombination of photo-induce electron-hole pairs and poor solar energy utilization as it absorbs only ultraviolet light (<4% of the solar spectrum) and precludes its application as a visible light photocatalyst [8]. Recently, bismuth based oxyhalides (BiOX) have been the focus of intensive study due to their unique and excellent photocatalytic, electrical and optical properties [9]. A great deal of effort has been devoted by the researchers to develop bismuth based catalysts with high photocatalytic activities for oxidation of water and the photodecomposition of organic dyes. In this regard, BiOCl may be most popular photocatalyst as its photocatalytic activity is comparable to TiO_2 under ultraviolet light irradiation [10]. Unique internal layered structure and high photocorrosion stability of BiOCl makes it ideal choice for further research and development in this field [11]. The photocatlytic efficiency of BiOCl is restricted for practical application by its intrinsic wide band gap (3.2–3.4 eV) that sternly limits viability as a visible light photocatalyst [12]. To alleviate this enduring issue attempts have been made by integrating BiOCl with other semiconductor components such as transition metals, transitions metal oxides, metal chalcogenides etc. and

---

designing a single heterostructure photocatalyst to reinforce the quantum efficiency of BiOCl [13–15]. Heterarchitechtured semi-conductor photocatalysts have acclaimed globally as a green and sustainable technology to degrade dyes under visible light for water remediation [16]. The enhanced photocatalytic efficiency, photostability and widen photoresponse of heterogeneous reinforced catalyst has been proven a thriving strategy and has been evident to manifest inherent strategies to suppress the photogenerated electrons and holes, recombination of charge carriers and enhance the probability of light harvesting and absorption of the base photocatalysts to the visible region [17,18].

In the last few years, to improve the wide absorption region in the visible light region and enhance mobility of charge carriers, the conjugated conducting polymers or their derivatives with Π-Π^* conjugated electron system have been used as prospective photosensitizer in BiOCl considering their good redox properties, low cost, chemically inert nature and easy facile synthesis [19–21]. Especially, Polyaniline (PANI) has demonstrated great promises due to its high absorption efficiency in the visible spectrum ($\lambda > 420$ nm) and mobility of charge carriers as well as enhancement of surface area [22,23]. Under visible light irradiation, PANI acts as an efficient electron donor as well as a good holes transporter [24]. A good design and incorporation of efficient heterojunction in photocatalysts with conducting polymers is significantly enhanced catalytic efficiency due to synergistic combination of functionalities. Many studies have shown combination of PANI with wide band gap semiconductors (like TiO$_2$, BiOCl and CdS) to improve their photocatalytic performance under visible light irradiation [25–27]. Hence, PANI based composites/hybrids with various semiconductors have become an emerging area of research for various photoelectric conversion applications.

Recently, numerous spinel ferrites (MFe$_2$O$_4$, M =Ni, Zn, Co, Mg, Ca) have attracted attention due to their photocatalytic properties as they demonstrated reasonable activity under visible light due to narrow band gap [28–30]. Also ferrites show good chemical stability, easy magnetic separation and low cost. It was found out that adsorption capacity, specific surface area and visible light driven photoactivity were improved by combining ferrites as codoped material with semiconductors such as BiOCl, TiO$_2$ and ZnO [31–33]. Doping of spinel ferrites onto semiconductors could extend the UV light absorption of BiOCl to the entire visible region by reducing its gap energy and it does enhance its photocatalytic activity in the degradation of organic pollutant [34,35]. In our previous study, we have reported the spinel structured dual phase nickel-zinc ferrite (Ni$_{0.5}$Zn$_{0.5}$Fe$_2$O$_4$) through co-precipitation method [36] and explored the enhancement of conductivity of polyaniline in presence of multiferrite [37]. Based on the recent developments in heterogeneous hybrid photocatalysts through incorporation of novel functionalised spinel ferrites as an efficient technology for degradation of organic pollutants specially reactive dyes, in the present study, we designed a novel hybrid heterostructure visible light responsive photocatalyst for water remediation by integrating Ni$_{0.5}$Zn$_{0.5}$Fe$_2$O$_4$@Polyaniline and a UV-sensitive photocatalyst BiOCl in view of the efficient utilization of sunlight. A simple facile chemisorptions method was used for the synthesis of Ni$_{0.5}$Zn$_{0.5}$Fe$_2$O$_4$@Polyaniline modified BiOCl (NPB) photocatalysts. Here we have hypothesised that (1) the doping of Ni$_{0.5}$Zn$_{0.5}$Fe$_2$O$_4$ nanocrystals as sensitive to magnetic field could facilitates catalyst separation from the aqueous dispersion as well as may promote visible light absorbtion (2) enhance light harvesting and photocorrosion inhibition due to enhanced conductivity of hybrid PANI [38] and (3) an interface formation between Ni$_{0.5}$Zn$_{0.5}$Fe$_2$O$_4$@Polyaniline and BiOCl and transit interfacial reaction process [39,40]. In our preliminary work it was found that the incorporation of as prepared polyaniline composite with low dose Ni$_{0.5}$Zn$_{0.5}$Fe$_2$O$_4$ (90:10) nanocrystals in BiOCl posses excellent

photocatalytic activity upon the degradation of methyl orange dye under visible light. To explored the technological importance and scientific realization of the commendable visible light driven photocatalytic activity of as-synthesized heterostructure composites, it's propitious performance was evaluated by the degradation of the four kinds of toxic dyes and relevant characterisations were carried out by employing XRD, UV–vis DRS, SEM-EDX, TGA, HRTEM, XPS, PL, BET and FTIR techniques. To scrutinize the admirable catalytic performance and harvesting of visible light by the established heterojunctions of PANI and multiferrite nanocrystals in BiOCl matrix, a possible mechanism has been sketched based on the effect of various scavengers on the degradation efficiency of the present novel photocatalyst and some earlier reported consequent analysis.

2. Experimental section

2.1. Materials

All chemicals were of analytical grade and used as received. Bismuth oxide (Bi$_2$O$_3$), aniline (ANI) monomer, sodium borohydride (NaBH$_4$), methyl orange (MO), congo red (CR) were purchased from Sigma-Aldrich, USA. Ammonium persulphate (AMPS), sodium hypochlorite (NaOCl), nickel chloride hexahydrated (NiCl$_2$·6H$_2$O), zinc chloride (ZnCl$_2$), anhydrous ferric chloride (FeCl$_3$) and ethanol (C$_2$H$_5$OH) were procured from Merck, Germany. NaOH, rhodamine B (Rh B), methylene blue (MB), HCl, TiO$_2$, methanol, tetrahydrofuran and ammonia solution were provided by SRL Pvt. Ltd., India. Double distilled water was used for preparation of all aqueous solution.

### 2.2. Methods

2.2.1. Synthesis of Ni$_{0.5}$Zn$_{0.5}$Fe$_2$O$_4$ (NZF)

Ni$_{0.5}$Zn$_{0.5}$Fe$_2$O$_4$ nanocrystals were prepared according to the previously reported procedure in an alkaline medium [36]. 1 M ferric chloride, 0.5 M zinc chloride and 0.5 M nickel chloride were mixed together in stoichiometric ratio. 0.5 M NaOH was poured into the mixture to maintain the pH above 12. The solution was continuously stirred at 1200 rpm for 4 h at 80 °C. The obtained dark brown precipitates were washed several times with methanol and double distilled water followed by overnight drying at 80 °C under vacuum.

2.2.2. Synthesis of Ni$_{0.5}$Zn$_{0.5}$Fe$_2$O$_4$ @ polyaniline nanofibers (NZF@P)

The Ni$_{0.5}$Zn$_{0.5}$Fe$_2$O$_4$@Polyaniline (NZF@P) nanofibers were synthesized by Chemical Polymerisation method [41]. A measured amount of NZF nanoparticles was dispersed in 100 ml of 1 N hydrochloric acid and kept in refrigerated orbital shaker at 5 °C. APS solution was prepared by dissolving in 25 ml of 1N HCl. APS solution and Aniline monomer was then added into the particle solution under shaking for half an hour. 4:1 ratio of aniline to APS was maintained. 2 ml of sodium hypochlorite (5 wt%) was also added dropwise. The appearance of green colour shows that polymerization has been started. Finally, the precipitates of NZF@P nanofibers were filtered and washed with HCl, double distilled water and acetone, and then freeze dried overnight.

2.2.3. Synthesis of BiOCl

BiOCl powder was prepared by a facile hydrolysis method [42]. About 2 gm of Bi$_2$O$_3$ was completely dissolved in concentrated hydrochloric acid solution. The white colloidal solution was obtained by adding aqueous ammonia solution into the above acidic solution to adjust pH value between 2 and 3. The colloidal solution was then heated at 40 °C for half an hour. White plates like precipitates of BiOCl were obtained. The precipitates were cen-
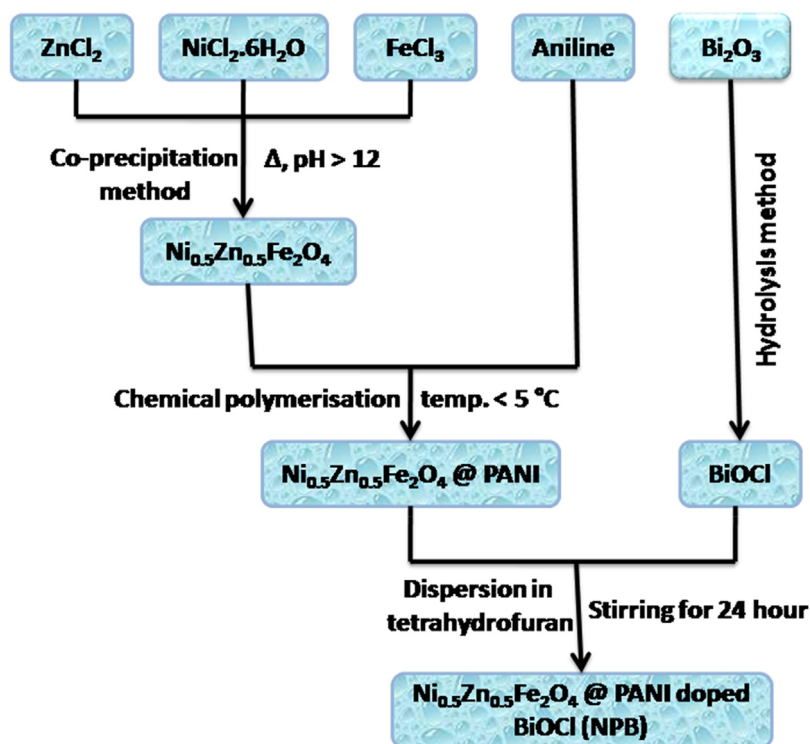
Scheme 1. Schematic representation for preparation of NZF@Polyaniline doped BiOCl composite.

trifuged and washed several times with ethanol and double distilled water. Finally, product was dried at 80 °C for 6 h in air oven.

2.2.4. Synthesis of $Ni_{0.5}Zn_{0.5}Fe_2O_4$ @ polyaniline modified BiOCl photocatalysts (NPB)

The $Ni_{0.5}Zn_{0.5}Fe_2O_4$ @ Polyanilie/BiOCl (NPB) photocatalysts were synthesized by dispersive mixing of NZF@P nanofibers and prepared BiOCl in tetrahydrofuran (THF). A stock solution of NZF@P was first prepared by dispersing NZF in THF with 0.45 g/l concentration. A measured amount of as-prepared BiOCl powder was added to 200 ml of the above NZF@P solution, then sonicated for 15 min, and finally stirred for 24 h. The suspension was filtered. The precipitates were washed by water and ethanol several times and transferred to oven to dry at 80 °C for 24 h. By changing weight percents of BiOCl, the composition of NZF@P was varied as 5 wt%, 10 wt%, 15 wt%, 20 wt% and 25 wt%, in different NPB composite samples and were named as NPB5, NPB10, NPB15, NPB20 and NPB25 respectively (Scheme 1).

2.3. Characterization

The X-Ray diffraction patterns of the composites were obtained on a Rigaku Ultima IV, X-ray diffractometer equipped with Cu Kα radiation having a wavelength of 1.54 Å. Each sample was scanned through a 2θ range of 10–90° at a rate of 8°/min. Fourier Transform Infrared (FTIR) spectra (KBr) were recorded on 3000 Hyperion Microscope with Vertex 80, FTIR spectrophotometer in the range 4000–400 cm^{-1} with 1 cm^{-1} resolution. The morphology and chemical composition of as-prepared composites were analyzed by a Zeiss model EVO40 scanning electron microscope equipped with an energy dispersive X-ray (EDX) spectrophotometer. A JEOL JEM 2100F transmission electron microscope was used to record high resolution images and particle size of the synthesized powders. Chemical state analysis was performed by X-ray photoelectron spectroscopy using Escalab 210 system, Germany, X-ray

photoelectron Spectroscope with a monochromatic Al Kα radiation source. The thermal properties were determined by a Q500 V20.10 Build 36 differential thermal analyzer (TG-DTA) in nitrogen atmosphere at heating ramp rate 10 °C min^{-1} upto 900 °C. The optical band gap energies of the powders were measured by UV–vis diffuse-reflectance spectra in wavelength range from 200 nm to 800 nm, obtained by Varian Cary 5000 UV–vis spectrophotometer. The photoluminescence (PL) spectra of the as-prepared composites were measured using a fluorescence spectrophotometer (F-4600, Hitachi). The Brunauer- Emmett- Teller (BET) method was used to determine the total surface area, pore volume and pore size of the prepared composites by physisorption of nitrogen on a Micrometrics ASAP 2010 analyzer based on the adsorption data in the partial pressure (P/P$_0$) range of 0–0.99. To measure photocatalytic activity and optical absorbance of dye solutions, Hitachi U-2900UV-vis spectrophotometer was used. TOC was measured on TOC analyzer (Shimadzu). CV and EIS analysis were performed on an Galvanostat potentiostat (SI 6143 instruments).

2.4. Photodegradation and adsorption measurements

2.4.1. Under visible light (artificial)

Catalytic activity of the as-prepared NPB photocatalysts were evaluated by the photodegradation of toxic dyes in a constant stirred cylindrical shaped photocatalytic quartz reactor. A 500 W halogen lamp (Philips, India) was used as the artificial visible light source. A suspension of 0.10 g synthesized photocatalyst in 100 ml of an aqueous solution of 10 mg/l MO dye (10 mg/l Rh.B, 10 mg/l MB and 10 mg/l CR) was stirred in dark for 1 h to establish an adsorption-desorption equilibrium. Then the solution was exposed to visible light located 20 cm away from the reaction solution. Cooling water was continuously circulated through an inner jacket of the reactor to invalidate heating effect of the visible light. After specific time intervals, 4 ml aliquots were withdrawn and centrifuged at 12000 rpm for 5 min to separate the photocatalyst powder. The
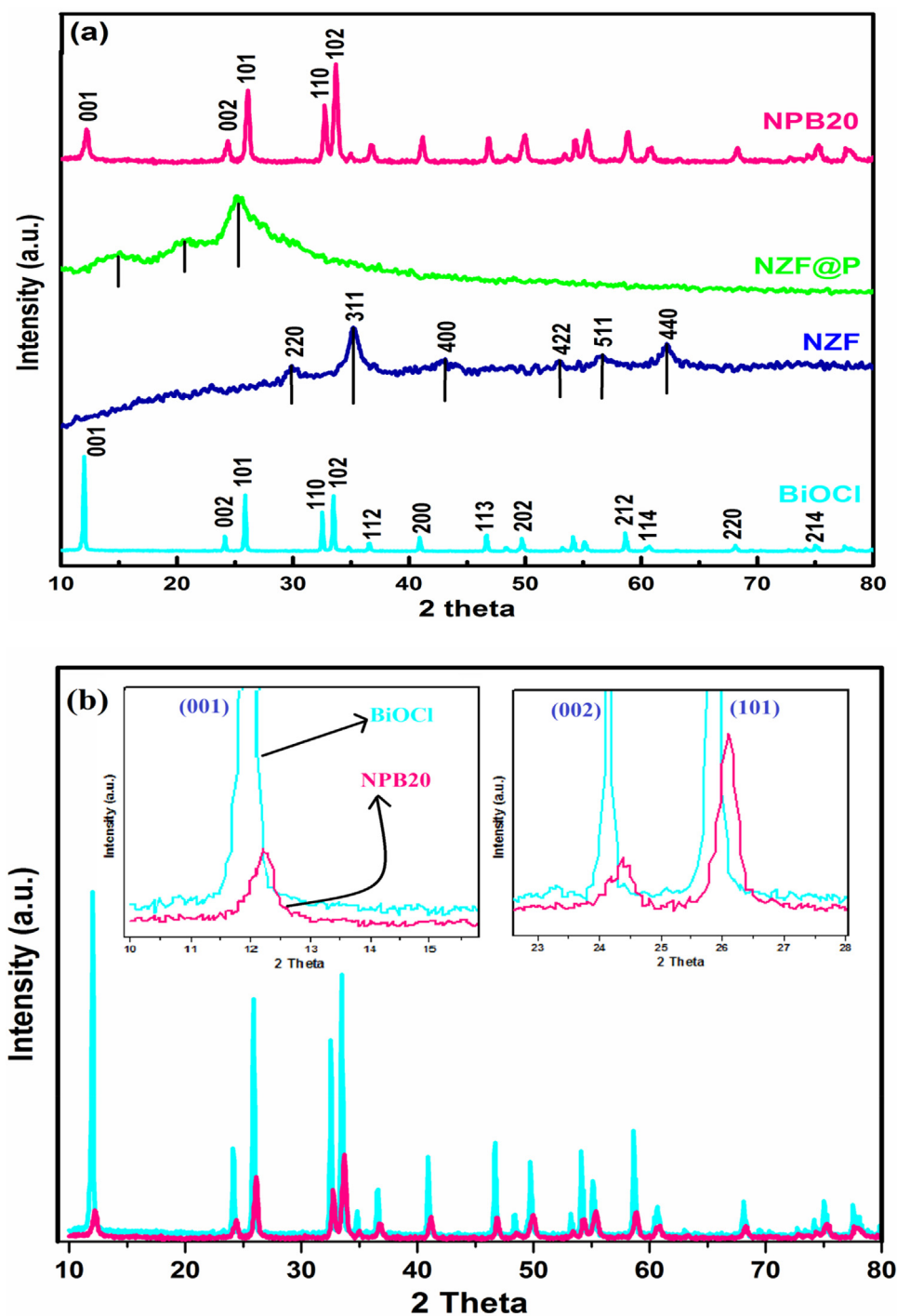
Fig. 1. (a) XRD pattern of pure BiOCl, NZF nanocrystals, NZF@P nanofibers and NPB20 composite; (b) slow scans of (001), (002) and (101) peaks of BiOCl and NPB20 composite (see inset figures).

Table 1
Band gap value and XRD analysis of BiOCl, NZF and NPB20 composite.

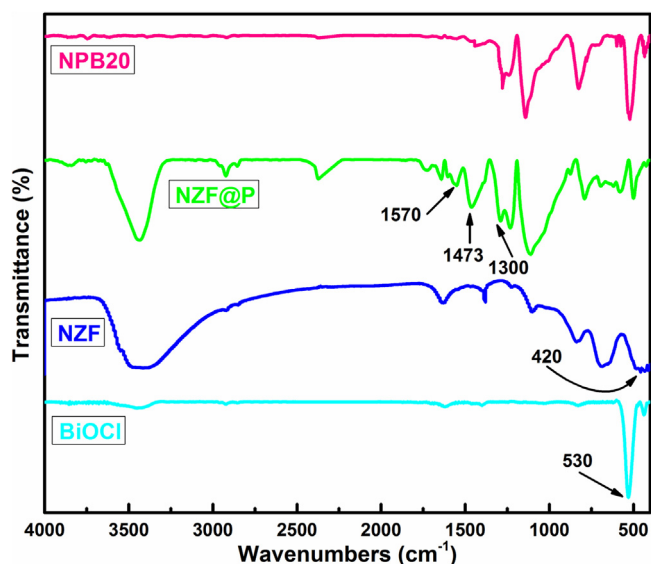| Sample	d-spacing values (Å)				Lattice constant (Å)	Average crystallite size(D, nm)	Band gap (E_g, eV)
BiOCl	7.387 (001)	3.689 (002)	3.442 (101)	2.676 (102)	a = b = 3.891, c = 7.369	78.49	3.2
NPB20	7.234 (001)	3.649 (002)	3.414 (101)	2.660 (102)	–	23.07	2.1
NZF	2.066 (220)	2.533 (311)	2.100 (400)	1.617 (511)	a = 8.346	7.92	0.8

"–" Not found.

Fig. 2. FTIR spectra of BiOCl, NZF, NZF@P nanofibers and NPB20 composite.

residual dye concentration in supernant was determined from the absorption band at λ_{max} = 464 nm (MO) using Hitachi UV–vis spectrophotometer. For adsorption measurements, the adsorption rate was calculated as

$$\text{Adsorption rate} = (a_0 - a)/a_{0 \times} 100\% \qquad (1)$$

where, a_0 and a are the absorbance values of dyes initially and after 1 h, respectively.

The degradation efficiency was calculated using the following equation:

$$\text{DE } (\eta \text{ \%}) = (A_0 - A)/A_{0 \times} 100\% \qquad (2)$$

where, A_0 and A are the absorbance values of dyes initially and after time t (min) of visible light irradiation, respectively. The same procedure was also carried out for synthesized BiOCl and procured TiO_2 for comparison. As well as, blank experiment was carried out without photocatalyst under visible light illumination.

2.4.2. Under solar light

The solar light dye degradation experiments were also carried out on bright sunlight. 200 ml of aqueous dye solution using same catalyst compositions were magnetically stirred in a glass beaker for 60 min under dark. Then the solution was exposed to sunlight from 11:00 a.m. to 4:00 p.m. on same day. Absorbance at different time intervals of the clear supernant was measured using UV–vis spectrophotometer.

2.5. Photocatalyst recyclability and stability

The recyclability experiments were performed for BiOCl and NPB20 using same methods as in 2.4.1 and 2.4.2 After each cycle, the photocatalyst was filtered and washed thoroughly with distilled water and absolute ethanol several times to remove residual dye impurities and then dried at 60 °C for 6 h. The recycled catalysts were successively used for four more runs of photocatalysis. The stability of the photocatalyst was also confirmed through SEM and XRD tests.

2.6. Reactive species study

Reactive species such as hydroxyl radicals ($^\bullet OH$), electron (e^-), holes (h^+) and superoxide radicals ($\dot{O}_2{}^-$) are main participants in the photocatalytic degradation process. In order to determine the

reactive radical species, trapping experiments were performed by adding various scavengers. Isopropyl alcohol (1.0 mM) was chosen as hydroxyl radical ($\dot{O}H$) scavenger, disodium ethylenediamine tetraacetate (1.0 mM) was chosen as the holes (h^+) scavenger, benzoquinone (1.0 mM) was chosen as the superoxide radical ($^\bullet O_2{}^-$) scavenger and silver nitrate (1.0 mM) was chosen as electrons (e^-) trapper. The trapping experiments were similar to the former photocatalytic activity test [43].

2.7. Analysis of hydroxyl radicals ($^\bullet OH$)

PL technique was used to detect hydroxyl radicals using terephthalic acid (TA) as probe molecule. During photocatalysis, terephthalic acid readily reacts with $^\bullet OH$ to produce highly fluorescent product, 2-hydroxyterephthalic acid.

$$^\bullet OH + TA \rightarrow TAOH \qquad (3)$$

The amount of $^\bullet OH$ radicals produced during photocatalysis is proportional to the luminescence intensity of 2-hydroxyterephtalic which was measured at 425 nm wavelength on a Hitachi F-7000 fluorescence spectrophotometer [44]. 0.1 g of as-synthesized NPB20 composite was dispersed in a 50 ml of the terephthalic acid aqueous solution (0.05 M in 0.02 M NaOH) in a constant stirred photocataltic reactor equipped with 500 W halogen lamp. PL spectra of the generated OH radicals were measured at 425 nm.

3. Results and discussion

For the optimization of NZF@P content, primary analysis of photocatalytic degradation of MO dye with different weight percent of NPB catalysts (0, 5, 10, 15, 20 and 25 wt%) was carried out. It was found out that catalyst loaded with 20 wt% of NZF@P was most efficient (Fig. 13b). Hence, 20 wt% of NZF@P (NPB20) was taken as the optimum concentration on BiOCl, and was characterized by XRD, FTIR, SEM-EDX, HRTEM, XPS, TGA, DRS, PL and BET surface area measurement.

3.1. Characterization

3.1.1. PXRD analysis

The phase composition and crystal structure of pure BiOCl, NZF nanocrystals, NZF@P nanofibers and NPB20 composite were confirmed by PXRD (Fig. 1a). The strong and narrow diffraction peaks of pure BiOCl at 11.98°, 24.10° and 33.4° match the (001), (101) and (102) planes of tetragonal BiOCl (a = b = 3.891 Å, c = 7.369 Å, JCPDS No. 06-0249) respectively indicating that the as-synthesized BiOCl was well crystallized [25]. The diffraction peaks of NZF nanocrystals at 2θ = 30.01°, 35.23°, 42.50°, 52.82°, 56.74° and 62.20° completely matched the reflections of (220), (311), (222), (400), (422), (511) and (440) planes, respectively, indexed to the spinel structure of $Ni_{0.5}Zn_{0.5}Fe_2O_4$ (a = 8.346 Å, JCPDS No. 08-0234)[36]. The XRD pattern of the NZF@P nanofibers revealed diffraction peaks at 13.30°, 20.60° and 25.40° corresponds to polyaniline [45] but the crystalline peaks of NZF nanocrystals are absent probably due to very small fraction of nanocrsytals. XRD pattern of as-prepared NPB20 composite shows strong and sharp peaks similar to BiOCl diffraction pattern but of lesser intensities. The intensity ratio I_{001}/I_{102} for NPB20 composite is 0.804, which is much smaller than that of I_{001}/I_{102} for BiOCl (1.7), hence (001) peak is no more dominanting for NPB20 composite. This ensures the doping of NZF@P nanofibers has decreased crystallinity of NPB20 composite. Also (001) peaks reveal a clear small shift towards larger angles (Fig. 1b) shows uniform dispersion of nanofibers.
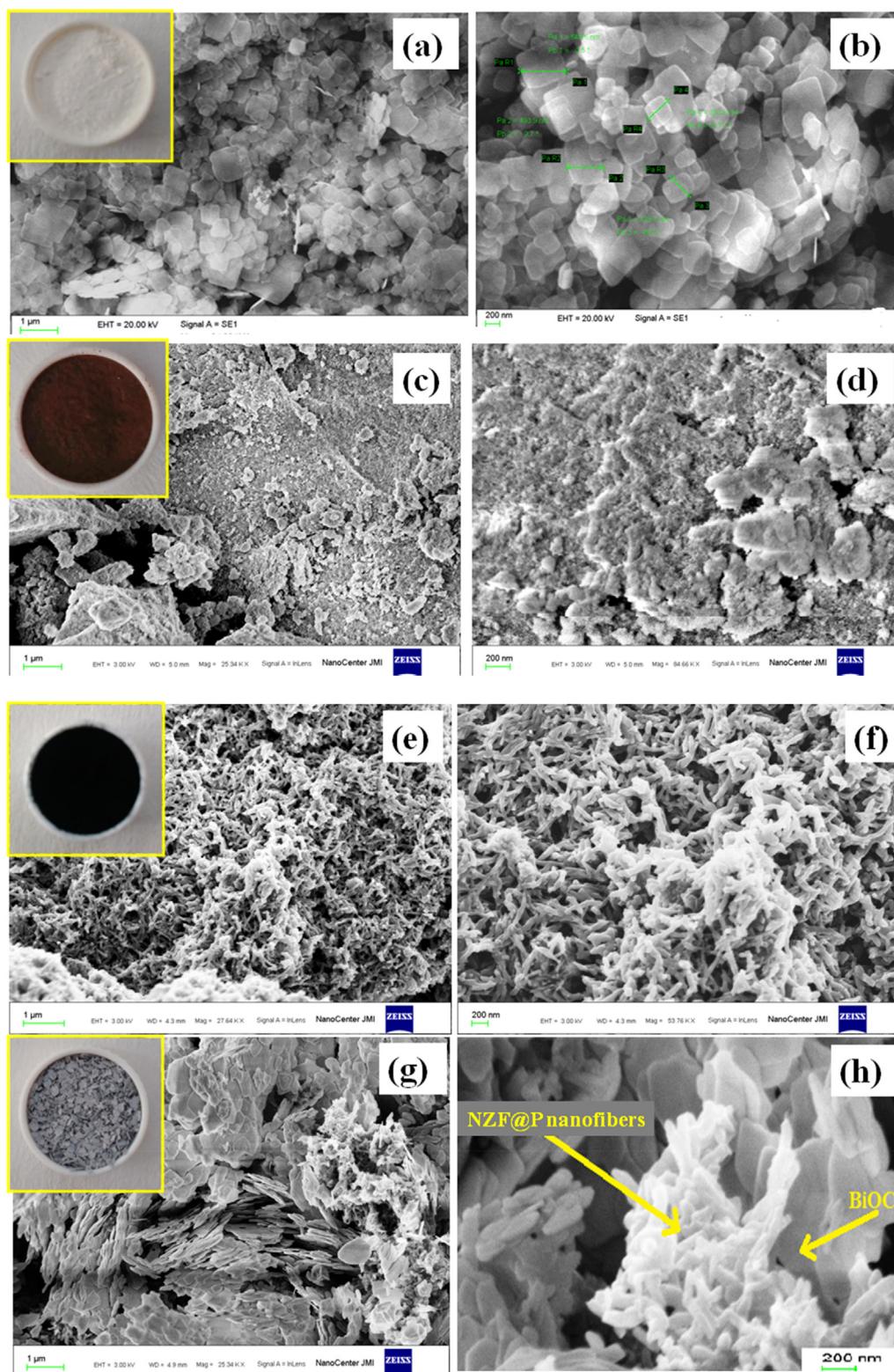
Fig. 3. SEM image of (a) BiOCl and FESEM images of (c & d) NZF, (e & f) NZF@P nanofibers and (g & h) NPB20 composite (inset pictures).

The average crystallite sizes of the pure BiOCl, NZF nanocrystals and NPB20 composite were estimated by using Debye-Scherrer equation:

$$D = k\lambda/\beta\cos\theta \tag{4}$$

Here, D is the crystallite size, k is a dimensionless factor, which is taken as 0.9, β is the full width at half maximum of the most intense diffraction peak of 001 plane for BiOCl, 311 plane for NZF nanocrystals and 102 plane for NPB20, respectively, λ is the wavelength of the Cu target (1.5406 Å), and θ is the Bragg diffraction angle. The d
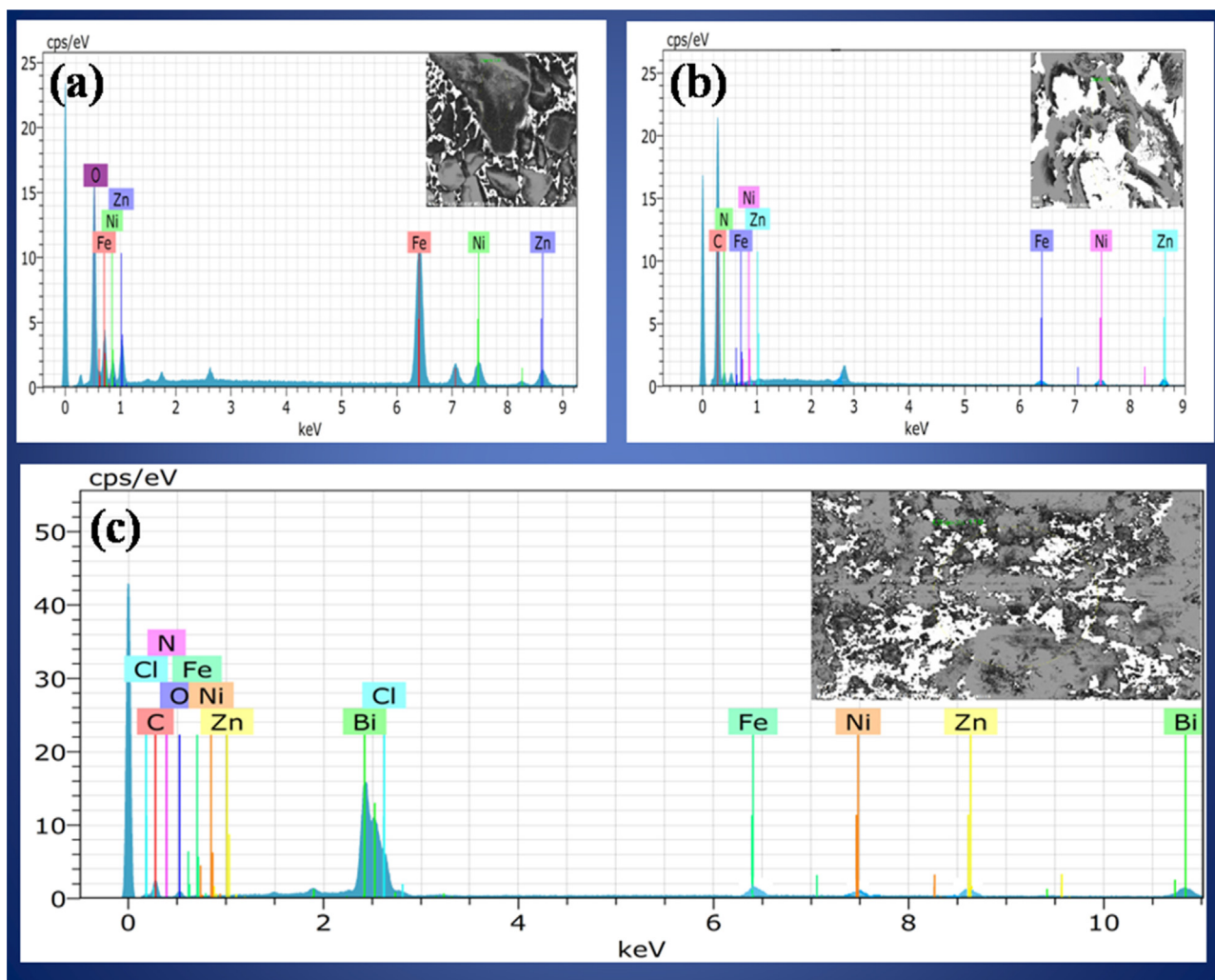
Fig. 4. FESEM- EDX spectrum of (a) NZF, (b) NZF@P nanofibers and (c) NPB20 composite.

values, lattice constants and the average crystallite size of the pure BiOCl and NPB20 composite are summarized in Table 1.

3.1.2. FTIR analysis

Fig. 2 shows the FTIR spectra of the pure BiOCl, NZF, NZF@P nanofibers and NPB20 composite. The IR spectrum of BiOCl shows intensive peak at $530\,cm^{-1}$ is assigned to the Bi-O bond [25]. FTIR spectra of the prepared NZF nanocrystals reveals weak band around $3444\,cm^{-1}$ attributed to stretching vibrations O—H from water molecules and characteristic peaks at $580\,cm^{-1}$ and $420\,cm^{-1}$ ascribed to intrinsic vibration of the tetrahedral and octahedral sites, respectively [36]. The peak intensities in the spectrum of NZF@P nanofibers are similar to the individual spectra of NZF and pure PANI peaks at $1570\,cm^{-1}$, $1473\,cm^{-1}$ and $1300\,cm^{-1}$. The NPB20 composite displayed characteristic peaks of PANI and BiOCl. But, NZF characteristic peak does not appeared which is due to low concentration of NZF nanocrystals.

3.1.3. SEM and EDS analyses

To study the morphology and structure, SEM images of BiOCl, NZF nanocrystals, NZF@P nanofibers and NPB20 composite were obtained. BiOCl mainly consists of a large number of two dimensional irregular plates with smooth surface [46] and thickness ranging from 35 nm to 45 nm (Fig. 3a & b). The bare NZF nanoparticles seem to be spherical in shape. A few agglomerates were also found (Fig. 3c & d). SEM images (Fig. 3e & f) show that NZF@P pos-

sesses fibrous structure and nanocrystals are also incorporated in those fibers. For NPB20 composite, Fig. 3g & h reveals that the deposition of NZF@P nanofibres makes the surface of BiOCl plates rough. Also the colour of BiOCl changes from white to grey after getting coated with NZF@P fibers.

EDX spectra of the samples were studied and the results are shown in Fig. 4. As shown in the EDX spectrum of the NZF nanocrystals (Fig. 4a), the peaks obtained ascribed to Ni, Zn, Fe and O elements. In the case of the NZF@P nanofibers, along with NZF components C and N elements were also found (Fig. 4b). In case of NPB20 composite (Fig. 4c), presence of Bi, O, Cl, N, H, Ni, Zn and Fe elements were also confirmed.

3.1.4. TEM analysis

The TEM results displayed in Fig. 5a, illustrate the dark brown NZF nanocrystals have spherical morphology with average diameter of 5–12 nm. TEM image of NZF@P nanofibers (Fig. 5b) inferred their fibre like structures and also showed that NZF nanocrystals are coated with polyaniline but some adhered on its surface. The NPB20 composite have similar images with the BiOCl nanosheets, except for the thin coating on the composite surface (Fig. 5c & d). This layer can be attributed to the introduction of NZF@P nanofibers. HRTEM studies (Fig. 5e & f) reveal the presence of lattice fringes with spacing of 0.250 nm accords well with (311) plane of NZF nanocrystals [36]. Results confirm the presence of randomly distributed fibrous structure over BiOCl.
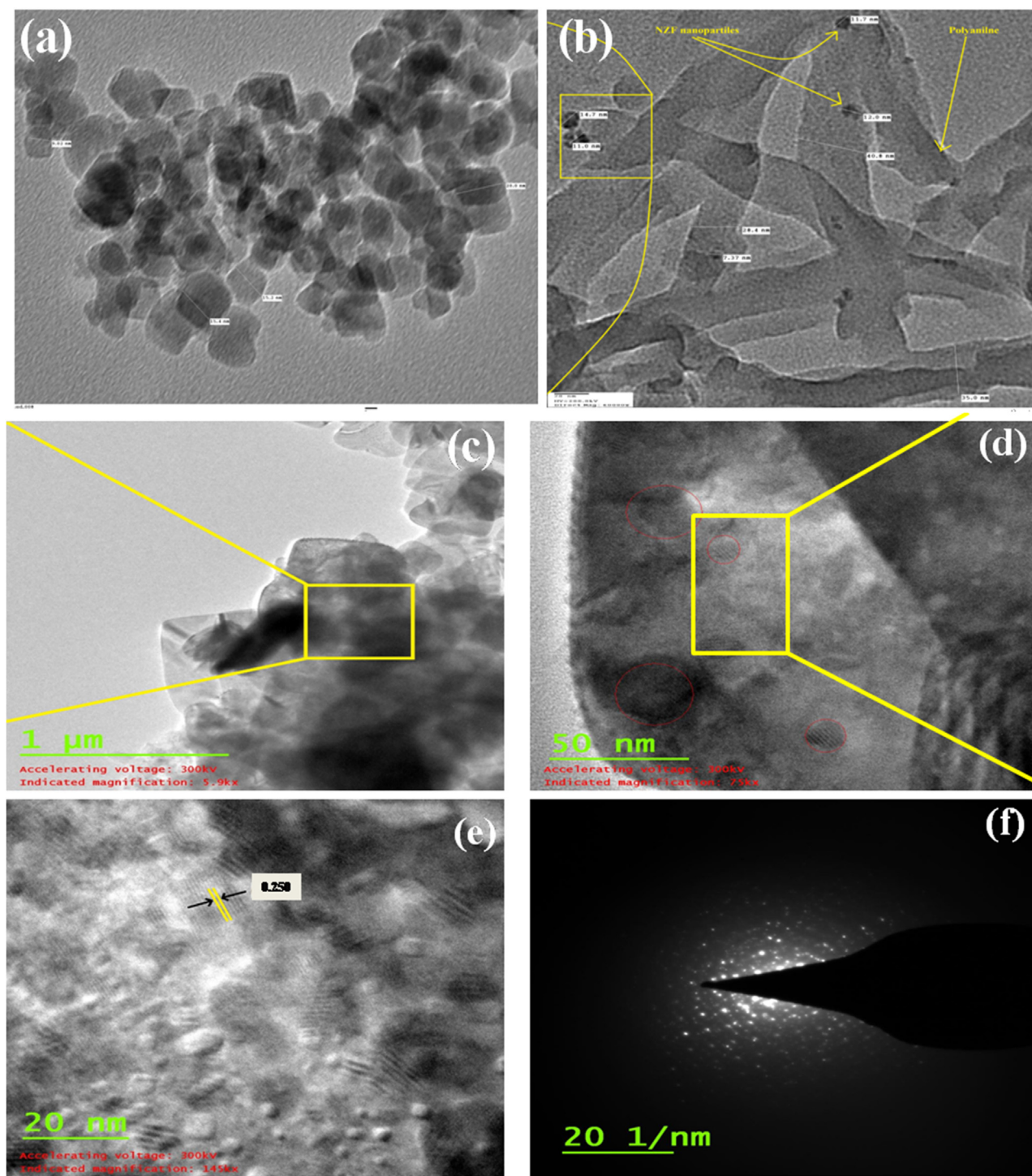
Fig. 5. TEM images (a & b), HRTEM image (c) and SAED diffraction pattern (d) of NPB20 composite.

3.1.5. XPS analysis

The XPS analysis of NPB20 composite was carried out to determine its element composition and chemical state. The survey XPS spectra (Fig. 6a) showed that the as-prepared NPB20 contained Bi, O, Cl, N, Fe, Ni and Zn elements. Fig. 6b shows two intense peaks at 159.1 and 164.9 eV which could be assigned to Bi $4f_{7/2}$ and Bi $4f_{5/2}$ respectively; indicating bismuth existed as Bi^{3+}. [47]. Diffused XPS signals for O 1 s (Fig. 6c) at a binding energy of 530.4 eV belongs to oxygen species of Bi-O bond. The peak at 198.4 eV corresponds to Cl 2p levels as the Cl $2p_{1/2}$ and Cl $2p_{3/2}$ energy levels overlapped and appeared as a single peak (Fig. 6d) [48]. In Fig. 6e, the N 1 s core spectrum shows diffuse peaks at around 399 eV with binding energy centered at 398.2 eV, 399.1 eV and 400.5 eV resulting from the quinonoid imine(-N-), benzenoid amine(-NH-) and imine(-NH⁺) groups respectively [49]. Fig. 6f shows the Fe 2p peak at 710.9 eV, which was consistent with the photoelectron peaks of Fe^{3+} in NPB20 composite [50]. Similarly, weak satellite peaks appeared at 854.5 eV and 1022.1 eV that corresponds to characterstic peaks of nickel and zinc, for Ni $2p_{3/2}$ (Fig. 6g) and Zn $2p_{3/2}$ (Fig. 6h) respectively [51]. The XPS analysis confirms the presence of BiOCl and NZF@P nanofibers in the NPB20 composite.

3.1.6. TGA analysis

Thermogravimetric analysis (TGA) curves of NZF, BiOCl, and NZF@P and NPB20 hybrids are shown in Fig. 7. The TGA curve of BiOCl is considerably stable and weight loss is almost negligible over a temperature range of 30–650 °C. Thermograms of NZF@P nanofibres show various stages of weight-loss. From 60–130 °C, approx 10% weight loss is due to expulsion of residual water molecules/solvents and during second step from 150 to 330 °C
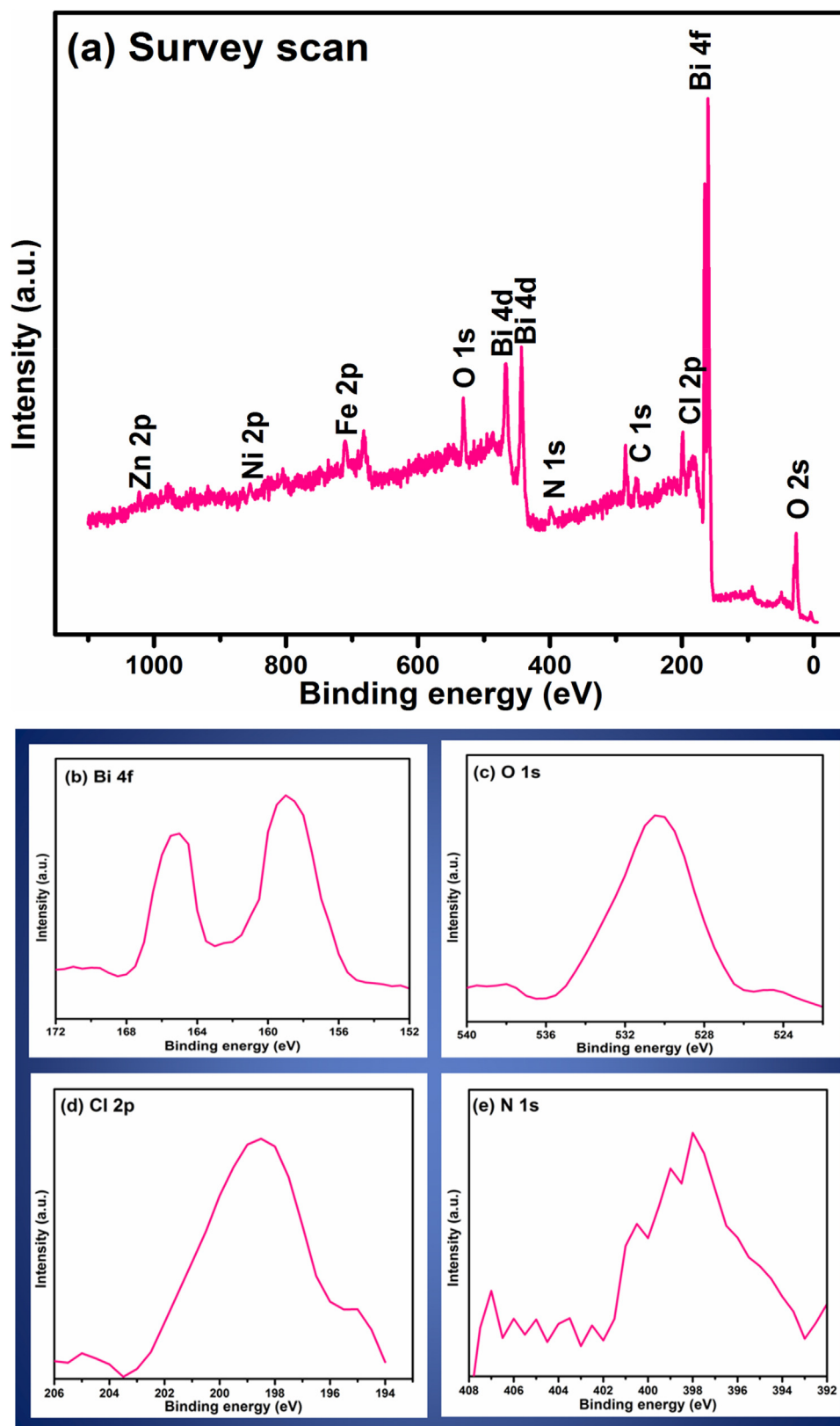

Fig. 6. XPS spectra of NPB20 composite (a) Survey scan, (b) Bi 4f, (c) O 1s, (d) Cl 2p, (e) N 1s, (f) Fe 2p, (g) Ni 2p, (h) Zn 2p, (i) C 1s.
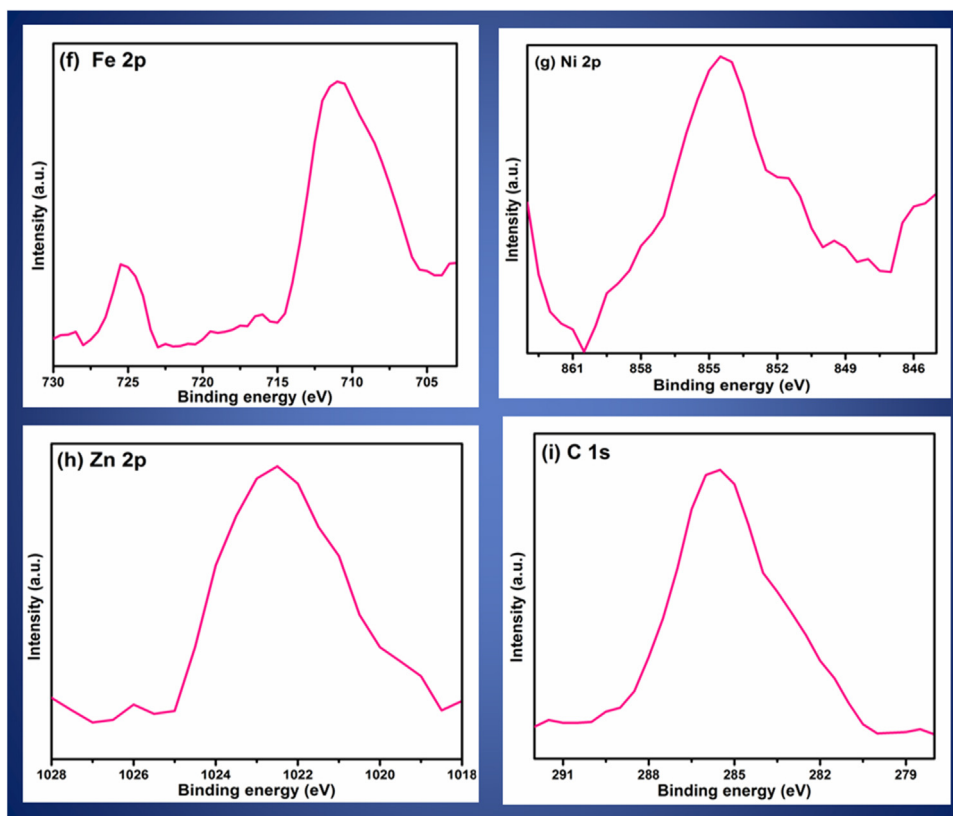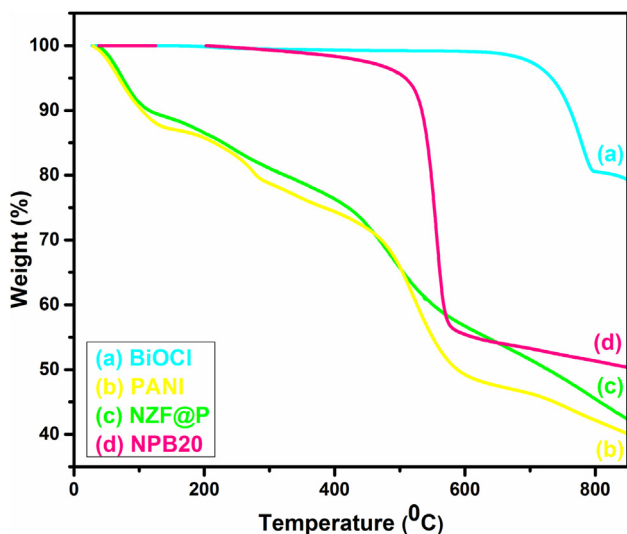
Fig. 6. (*Continued*)

Fig. 7. TGA analysis of (a) BiOCl (b) PANI (c) NZF@P nanofibers and (d) NPB20 composite.

shows thermal degradation of the low weight oligomers and from 380 to 600 °C the major wt loss of approx 24% is due to the thermal degradation of the polymer formed and the last degradation is due to the nanoparticles present in the NZF@P. Overall PANI shows approx 52% weight loss. From the TGA curves of BiOCl and NPB20 hybrid, it could be seen that both samples exhibits similar behaviour but distinctive weight loss starts at 650 °C in BiOCl but starts at 400 °C for composite and which is because of the presence of NZF@P nanofibers in the NPB20 composite. So compared

to BiOCl, NPB20 degrades earlier at 450 °C where as BiOCl is quite stable upto that.

3.1.7. BET analysis

The Brunauer-Emmet-Teller surface area and pore size distribution of the prepared photocatalysts were investigated using nitrogen adsorption desorption measurements. Fig. 8a & b displays N$_2$ adsorption-desorption isotherms of bare BiOCl and 20% NZF@P nanofibers doped BiOCl nanophotocatalyst. It is clearly observed that the isotherms belong to type-IV isotherms, indicating as-prepared samples were mesoporous materials [52]. The BET surface area and pore volume (single point, P/P$_0$ = 0.951) of the composite is 18.45 m^2/g and 0.021 cm^3/g respectively, which are higher than pure BiOCl (BET = 6.02 m^2/g and pore volume = 0.012 cm^3/g). As well as average Barrett-Joyner-Halenda pore diameter distribution of BiOCl and NPB20 are given in inset Fig. 8a & b, respectively. An increase in BET surface area of as-prepared composite is due to incorporation of doped material. Therefore, NPB20 have more surface active sites and provides easy charge transportation, leading to enhanced photocatalytic activity of the prepared composite [53]. The increase in activity of NPB20 was further proved by enhanced value of degradation rate constant 'k' (Fig. 11d).

3.1.8. Photoluminescence analysis

Photoluminescence technique is commonly used to study recombination rate, life span and behaviour of photogenerated electron-hole pairs [54]. Fig. 9 shows the photoluminescence emission spectrum of as-prepared BiOCl and NPB composites at room temperature. The excitation light source is a 280 nm He-Cd laser. The emission peak for BiOCl was observed at around 320 nm under visible light. NPB composites showed weaker emission peaks, indicating introduction of NZF@P nanofibers improved the separation efficiency and lowered down the recombination rate of electron-
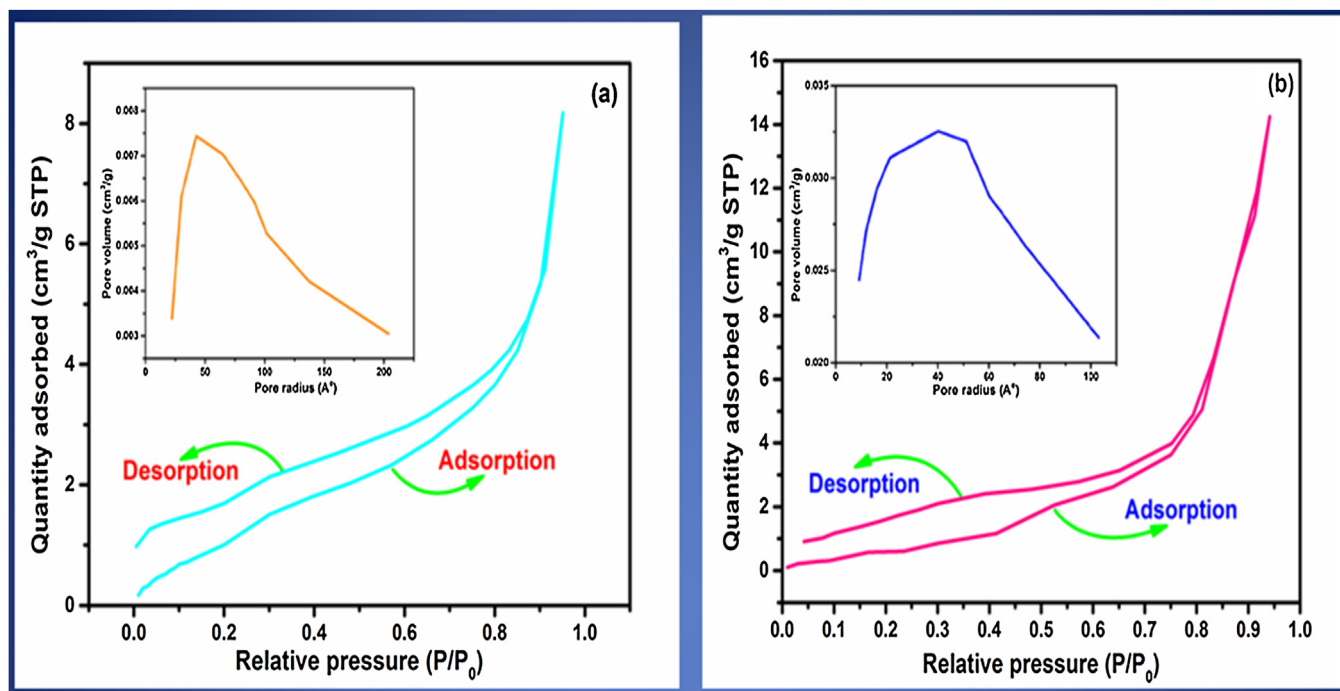
Fig. 8. Nitrogen adsorption-desorption isotherm and pore size distribution (inset) of (a) pure BiOCl and (b) NPB20 composite.
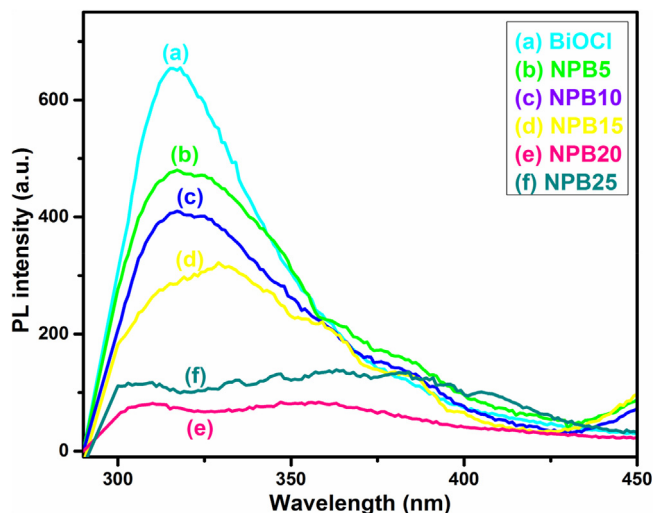

Fig. 9. Photoluminescence spectra of the (a) BiOCl, (b) NPB5, (c) NPB10, (d) NPB15, (e) NPB20 and (f) NPB25 composites (excitation wavelength 280 nm at room temperature).

hole pairs under visible light. Among these, NPB20 showed the weakest peak and hence is the most efficient. It can be concluded that decreased rate of electron-hole recombination ensures more photons utilization during photocatalytic reaction. Thus a better photocatalytic performance can be achieved and was proven by photocatalytic activity experiments (Fig. 11b).

3.1.9. UV–vis DRS

The DRS is a useful tool for calculating band gap of materials. The optical diffuse reflectance spectra of bare BiOCl, NZF, NZF@P and NPB compositions (NPB15, NPB20 and NPB25) are displayed in Fig. 10a. All these spectra are recorded in the wavelength range of 200–800 nm at room temperature. The optical absorption edge of the pure BiOCl was roughly estimated at about 320 nm respectively. NZF@P nanofibers show strong and broad absorption in the visi-

ble region around 635–660 nm. All three NPB composites exhibit almost the same absorption profile as BiOCl with a visible absorption region from 380 nm to 410 nm. A slight red shift was also noted for NPB20 and NPB25 (from 419 to 440 nm). It is a good evidence for superior interaction between BiOCl and NZF@P [55,56]. Moreover, the color of the NPB heterojunctions changes from white to grey (inset Fig. 3a, c, e, f) with loading NZF@P. Since BiOCl had no absorption in the visible region, the visible light absorption of NPB composites was only due to the contribution of polyaniline and NZF nanocrystals.

The band gap of a semiconductor could be calculated by the following equation.

$$\alpha h\upsilon = \frac{A(h\upsilon - Eg)^n}{2} \tag{5}$$

Where, A, α, Eg and υ are proportional constant, absorption coefficient, band gap and light frequency respectively. Among them, n depends on the characteristic transition in semiconductor (i.e, n = 1 for direct transition or n = 4 for indirect transition). For BiOCl, the value of n is 4 for indirect transition. The band gaps of the samples were estimated with the energy intercept of a straight line fitted through the rise of the Kubelka Munk function plotted versus energy of absorbed light E [57]. The intercept of the tangent to the X-axis will give a good approximation of the band gap energy for the photocatalyst (Fig. 10b). The band gap of NZF@P and BiOCl were 1.2 and 3.2 eV whereas, the band gap of NPB15, NPB20 and NPB25 were 2.82 eV, 2.1 eV and 2.02 eV respectively. It is observed as the concentration of NZF@P nanofibers increased in NPB composites, the calculated value of band gap decreased. This reduction in band gap proves to enhance photocatalytic activity under visible light as efficient utilization of solar energy could be possible.

In the composites, the photocatalytic activity can be best explained from the valence band (VB) and conduction band (CB) positions of the constituent semiconductors and was calculated from the following equations:

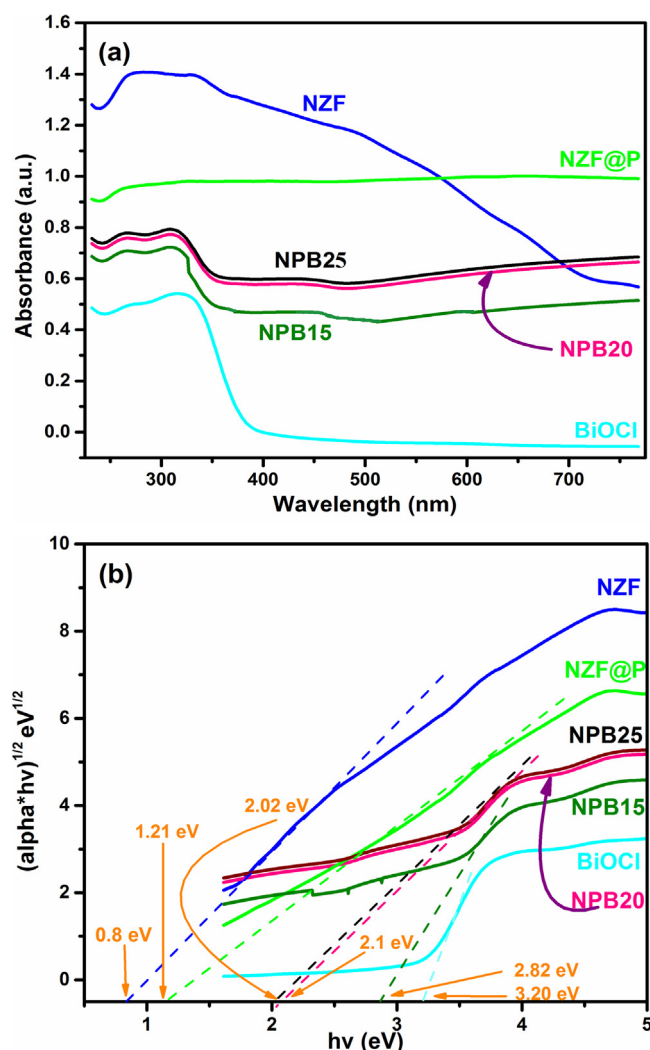$$E_{CB} = X - E_e - 0.5E_g 0.5E_g \tag{6}$$

$$E_{VB} = E_{CB} + E_g \tag{7}$$

Fig. 10. (a) UV–vis diffuse relectance spectra and (b) plot of $(\alpha h\upsilon)^{1/2}$ versus $h\upsilon$ for the band gap energies of the BiOCl, NZF, NZF@P, NPB15, NPB20 and NPB25 composites.

Where X is the electronegativity of the semiconductor, which is the geometric mean of the electronegativity of the constituent atoms, E_e is the energy of the free electrons on the hydrogen scale (4.5 eV) and E_g is the band gap energy of the semiconductor.

3.2. Photocatalytic performance

3.2.1. Photocatalytic performance for MO degradation under visible and solar light

The photocatalytic performances of the synthesized composites were initially evaluated by MO degradation under visible light irradiation. The TiO_2 (P25) was chosen as control photocatalyst under visible light, as it is the most efficient commercial available photocatalyst. Fig. 11a shows saturated adsorption capacities of MO on the surface of pure BiOCl, TiO_2 and various NPB composites under dark. The NPB composite with 20 wt% and 25 wt% of NZF@P nanofibers shows high saturation adsorption ability (about 24.04% and 24.84%) than the pure BiOCl and TiO_2 (about 3.69% and 2.55%). As the visible light was applied, the photodegradation of MO dye started (Fig. 11b). During photolysis, negligible degradation of dye (only 5%) was observed even after 60 min. It is very clear that each of the pure BiOCl, NZF and TiO_2 shows poor activity under visible light whereas all the NPB composites exhibit stronger photodegradation activity for MO. Amongst the NPB composites, NPB20 showed

the highest photoactivity and degraded the MO dye almost completely within 60 min of visible light irradiation. To confirm the MO has really degraded, we tested the Total organic carbon (TOC) of MO solution over NPB20 composite, which reflects the extent of mineralization of organic species [58]. The initial TOC of the MO solution is 17.1 mg/l, after 1 h visible light irradiation the TOC concentration decreases to 3.7 mg/l. Therefore, in our experiments, the reduction of TOC further confirms that MO is truly photodegraded by the NPB20 photocatalyst instead of simply decolored.

Temporal evolution of the spectral changes during the decolorization of MO using NPB20 is displayed in Fig. 11c. It is found that the peak intensity at 464 nm gradually decreases without the appearance of any other new peak, which confirmed the absolute decomposition of MO.

The degradation reaction kinetics was studied over the different NPB composites by using pseudo first order kinetic model.

$$-\ln\left(\frac{C}{C_0}\right) = k_{app} \times t \tag{8}$$

Where, k_{app} is the apparent rate constant (min^{-1}), C_0 and C are the concentration of dye initially and at time t (min), respectively. The variations in concentration as a function of irradiation time are given in Fig. 11d. It is found that the NPB20 heterostructure exhibit the highest degradation rate as the k_{app} of the NPB20 heterostructure is about 7.5 times higher than that of BiOCl and 30 times higher than that of TiO_2. The enhancement in photocatalytic activity is attributed to the surface oxidation – reduction reactions, high photon absorption rate, and generation of electron-hole and separation-migration of active charge carriers [59].

The ultimate aim of developing visible light active catalysts is to utilize natural solar light. Therefore, we also tested the photoactivity of the developed NPB composites under natural sunlight for the degradation of MO. The NPB20 heterojunctioned composite showed excellent photocatalytic activity under these conditions, with the degradation efficiency of 91.56% within 75 min (Fig. 11e). The rate constant values for the composites are given in inset Fig. 11e. The developed heterocomposite shows higher photocatalytic degradation efficiency than others reported work for the removal of MO dye (Table 2)

3.2.2. Photocatalytic performance for Rh.B, MB and CR under visible and solar light

Further, photocatalytic activity of NPB20 composite was evaluated with different types of model pollutants such as MB, CR and Rh.B under visible light (Fig. 11f–h) and natural sunlight (Fig. 1i). The photodegradation results indicated that NPB20 composite for the photodegradation of RhB, CR and MB were also much higher than that of the pure BiOCl under visible and sunlight.

3.3. Recyclability of the photocatalyst

It is very important to explore the recyclability and photostability of the photocatalyst for its practical applications. For that we carried out four recycle runs of photodegradadtion of MO on BiOCl and NPB20 composite.

3.3.1. Stability under visible light irradiation

The photocatalyst was centrifuged, washed with distilled water and ethanol, and dried in an oven at 60 °C after each run. As for the BiOCl, no significant loss of photocatalytic activity during visible light irradiation is observed even after fourth cycle whereas the photocatalytic decolorization by NPB20 composite decreases slightly after each run (Fig. 12a). The decrease in photocatalytic activity is due to the adsorption of some organic compounds on the surface of the catalyst, which block the active sites and change the structure of the catalyst. XRD and SEM results of BiOCl and NPB20

Table 2
Comparison of photocatalalytic degradation of MO dye with different photocatalyst system.

Photocatalyst	Irradiation source	Decolorisation time	Dye conc.	Amount of catalyst	% Removal	Ref.
NPB20	Halogen, 500 W	60 min	10 mg/l	1 g/L	96.5	This work
PANI modified TiO$_2$	Xenon, 500 W	360 min	10 mg/l	1 g/L	96	22
PANI/BiOCl	Xenon, 500 W	210 min	10 mg/l	1 g/L	67	25
BiOCl	Xenon, 500 W	120 min	10 mg/l	0.8 g/L	79	56
BiOI/BiOCl	Halide, 300 W	180 min	20 mg/l	0.5 g/L	95	57
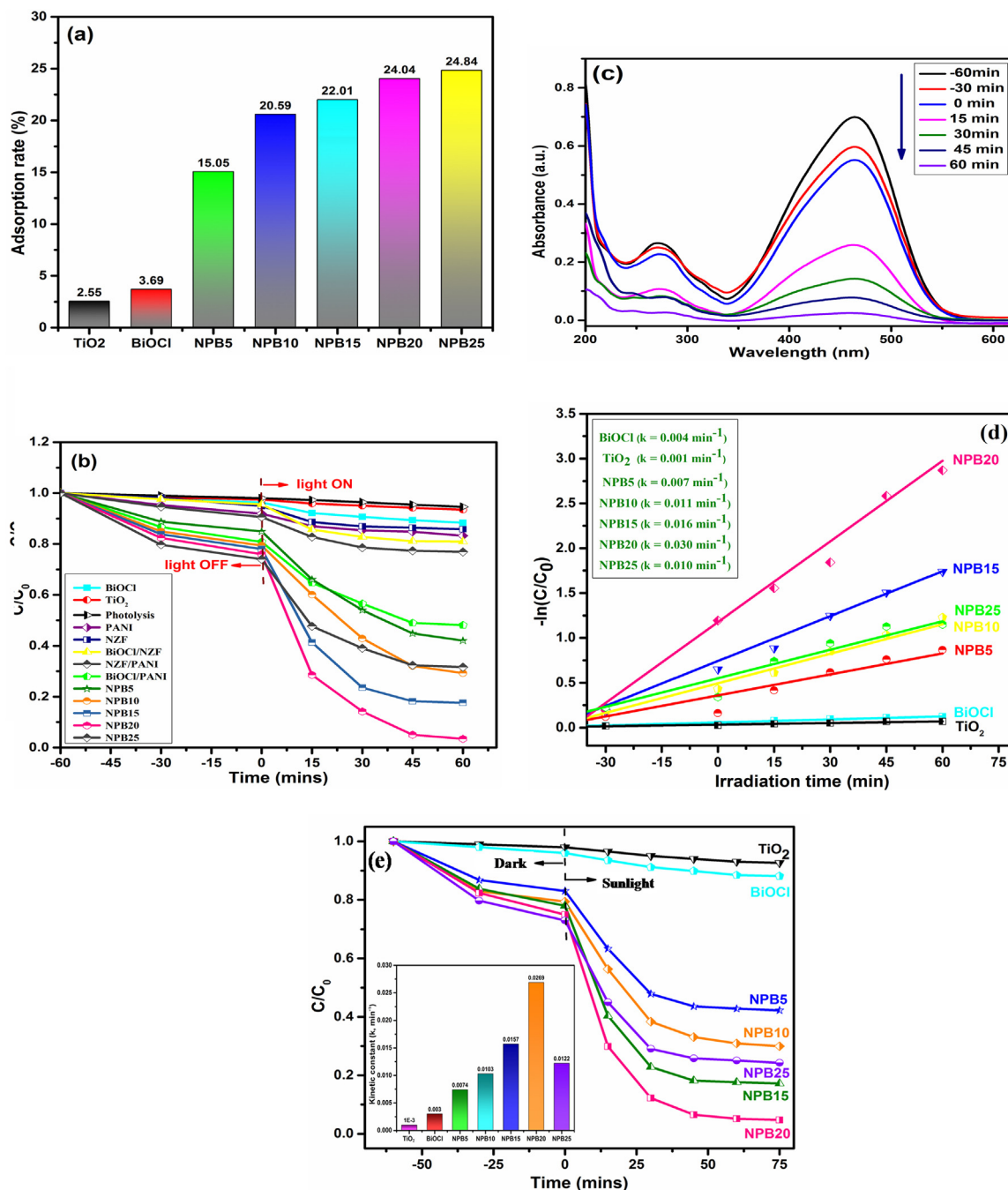
Fig. 11. (a) Adsorption rate% of TiO$_2$, pure BiOCl and various NPB composites for MO, (b) Photocatalytic degradation activity for MO under visible light($\lambda > 420$ nm) irradiation over pure BiOCl, TiO$_2$, pure PANI, pure NZF, BiOCl/NZF, BiOCl/PANI, NZF/PANI, NPB5, NPB10, NPB15, NPB20 and NPB25 composites, (c) UV–vis absorption spectral changes of MO (10 mg/l, 100 ml) in the presence of NPB20 composite (0.1 g) under visible light ($\lambda > 420$ nm), (d) Kinetic plots for photocatalytic degradation of MO over BiOCl, TiO$_2$, NPB5, NPB10, NPB15, NPB20 and NPB25, (e) Photocatalytic degradation activity for MO under sunlight over pure BiOCl, TiO$_2$, NPB5, NPB10, NPB15, NPB20 and NPB25 composites and Photocatalytic degradation of MB (f), CR (g) and RhB (h) in the presence of BiOCl and NPB20 under visible light and (i) degradation efficiency of BiOCl and NPB20 for MB,CR and RhB under solar light.
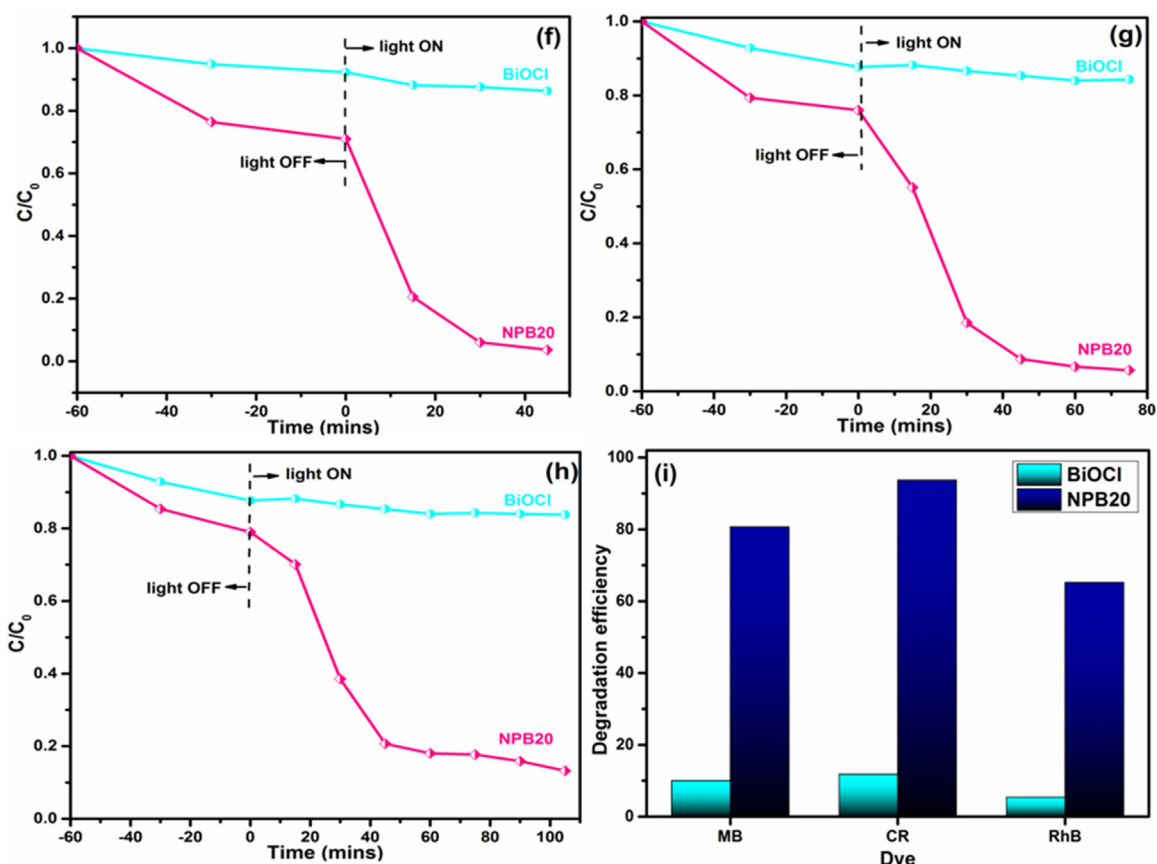
Fig. 11. (*Continued*)

photocatalysts obtained after four recycles were also carried out. XRD results (Fig. 12b & c) confirm that phase and structure of both the catalysts remained unchanged. Moreover, SEM images of the recovered photocatalyst were barely changed (Fig. 12d & e). Results clearly indicated that the NPB20 is an ideal photocatalyst for the practical applications in the wastewater treatment.

3.3.2. Stability under solar light irradiation

Stability of BiOCl and the NPB20 photocatalysts were also investigated for MO degradation under natural sunlight irradiation repeating the reaction four times for 60 min (Fig. 12f). The degradation efficiency of NPB20 changes a little, even after four recycle runs. These results indicated that NPB20 photocatalyst has a reasonable stability even under natural sunlight.

3.4. Mechanistic outlooks for photocatalytic degradation of MO under visible light

It is well accepted that the photocatalytic activity of the catalyst are highly affected by the adsorption capacity and the separation efficiency of photogenerated electron-hole pairs [60,61]. From the adsorption degradation curves it is clearly indicates that positively charged PANI can be adsorb anionic dye (MO) effectively and leads higher rate of degradation.

It is comprehended that the origin for photocatalytic degradation by the semiconductors is underlying the redox reaction on the catalyst surface by the separated charge carriers i.e., electrons and holes [62,63]. The generated active species such as hydroxyl radicals (OH) and superoxide radical ions ($O_2^{\bullet-}$) by the redox reaction are participated in oxidative degradation of the absorbed dye molecules on the catalyst surface [64]. Therefore to understand the

factors affecting for the efficient photocatalysis by the composites NPB20 over other catalysts under visible light we have performed the active species trapping experiments and photoluminescence spectral analysis.

Fig. 13 displays the trapping experiment of active species during the photocatalytic reaction. It can be seen that the photocatalytic degradation of MO was remarkably decreased after the addition of EDTA-2Na and IPA. This suggests that the holes directly reduced dye molecules as well as react with the adsorbed water (or hydroxide anions) to yield hydroxyl radicals, and oxidize MO. So, holes and hydroxyl radicals are the main active species in this system. However, addition of benzoquinone and AgNO$_3$ does not have considerable effect on photocatalytic activity of the NPB20 composite. Therefore, it can be deduced that the MO degradation is mainly due to the holes and hydroxyl radicals, and electrons and superoxide radicals have weak influence.

In order to detect the hydroxyl radicals produced during photocatalysis reaction, PL technique was used. The PL emission spectra excited at 315 nm from terephthalic acid solution was noted after every 15 min of visible light irradiation. For BiOCl, almost negligible peaks were detected whereas a gradual increase in peak intensity was observed for NPB20 composite as the visible light irradiation time increases from 0 to 60 min (Fig. 14). This indicates that the fluorescence is caused by chemical reactions of terephthalic acid with •OH formed on the NPB20/water interface via photocatalytic reactions [65]. It also confirms the presence of •OH radical as main active species for photocatalytic degradation of MO dye. It suggested that NZF@P nanofibers could be considered as strong visible light photosensitizers for BiOCl.

The heterojunction between semiconductor and PANI have showed the remarkable synergistic effect for the efficient sep-
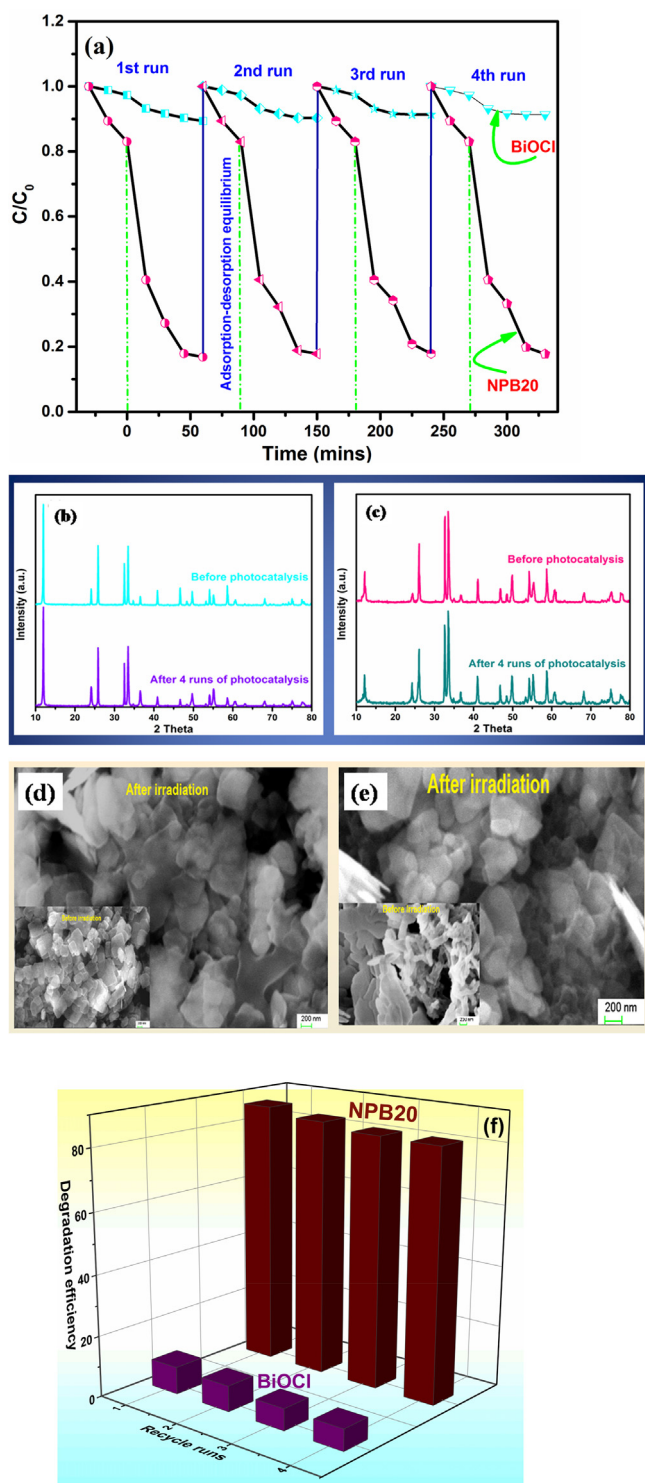
Fig. 12. (a) Reusability of the NPB20 composite for four successive runs, (b–c) XRD patterns of before and after the photocatalytic degradation reaction of BiOCl and NPB20, (d–e) SEM images of BiOCl (d) and NPB20 (e) before and after the photocatalytic degradation reaction and (f) Reusability of BiOCl and NPB20 under solar light (MO degradation).
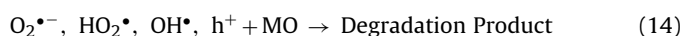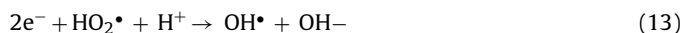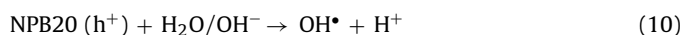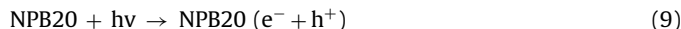
aration of photogenerated electron-hole pair and attributed a significant enhancement in photocatalytic activity for the dye degradation. Many researchers have explained the individual role in heterojunctured catalysts and reported that the combination of semiconductor (like TiO_2), multiferrite (like $CoFe_2O_4$) and PANI substantially improves the separation efficiency of photogener-

ated electron-hole pairs provided by their photosynergistic effect [60,66]. Electrochemical impedence spectroscopy (EIS) and cyclic voltameter measurement were carried out for a better understanding of the synergistic effect and also may be useful in helping to support the highest photocatalytic activity of NBP20.

EIS was a fundamental tool for characterizing the interfacial charge transfer properties of electrodes. Generally, the diameter of semicircle in the Nyquist plot was equal to the charge transfer resistance of the electrode surface and a smaller diameter means a lower resistance [67]. Fig. 15 displayed the Nyquist plot for the prepared BiOCl and NPB composites. It was found that NPB20 has a low resistance value as compared to BiOCl that was consistent with the results of PL analysis. Finding indicates that a faster interfacial charge transfer leads to an effective separation of electron-hole pairs due to incorporation of NZF@P composite nanofibers [68].

The cyclic voltammeter (CV) responses of pure BiOCl and NPB composites were recorded in 5 mM of $[Fe(CN)_6]^{3-/4-}$ containing in 0.1 M KCl at a scan rate of 5 mV/s. As shown in Fig. 16 as NZF@P percentages increases the current response at concentrations upto 20 wt% also increases, however at concentration greater than 20 wt% NZF@P, the current responses decreases. It demonstrates that the redox peak of the NPB20 composite higher as compare to other compositions. It again concludes that NPB20 provides appropriate electronic channel and enhances separation of photoelectrons and holes as already supported by EIS and PL studies. Very recently it is reported that the presence of PANI in the heterostructured composite electrodes of BiOCl had good electrochemical performance due to its unique hierarchical structure, a shortpathway for ion penetration and a connection to the PANI chains by ionisable BiOCl [69].

Based on the results from the PL and trapping experiments, we have proposed a tentative photocatalytic reaction mechanism for the NPB20 photocatalysts (Scheme 2). It can be found that BiOCl cannot absorb visible light ($\lambda > 420$ nm) because of its large band gap (3.2 eV) whereas NZF nanocrystals and PANI can produce electrons and holes. Under visible light, both PANI [70] and NZF [71] can absorb photons to generate electron-hole pairs. The photogenerated electrons in the CB of NZF can readily inject into the LUMO of PANI and then transfer into the CB of BiOCl. However, electrons on the CB of BiOCl cannot react with O_2 to produce $^\bullet O_2^-$ as CB potential of BiOCl (0.11 eV vs NHE) is more positive than E_0 ($O_2/^\bullet O_2^-$) (-0.046 eV vs NHE) [72]. Simultaneously, photogenerated holes in the VB of BiOCl transfer into the HOMO of PANI and further transfer to the VB of NZF. As a result, a rapid charge separation and slow charge recombination occur and any transferred charge carriers may participate in the subsequent redox reactions with either the oxidants or the reductants in the solution, thereby resulting in higher photocatalytic activity [73]. A possible reaction path for redox reaction is as follows:

$$NPB20 + h\nu \rightarrow NPB20\ (e^- + h^+) \tag{9}$$

$$NPB20\ (h^+) + H_2O/OH^- \rightarrow OH^\bullet + H^+ \tag{10}$$

$$NPB20\ (e^-) + O_2 \rightarrow O_2^{\bullet-} \tag{11}$$

$$O_2^{\bullet-} + H^+ \rightarrow HO_2^\bullet \tag{12}$$

$$2e^- + HO_2^\bullet + H^+ \rightarrow OH^\bullet + OH- \tag{13}$$

$$O_2^{\bullet-},\ HO_2^\bullet,\ OH^\bullet,\ h^+ + MO \rightarrow \text{Degradation Product} \tag{14}$$

4. Conclusions

Interfacial junctions between $Ni_{0.5}Zn_{0.5}Fe_2O_4$@Polyaniline and BiOCl via a facile chemisorptions method and transit interfacial reaction process provide a pathway for tailoring low energy photon absorption and reduction in recombination rate of light induced
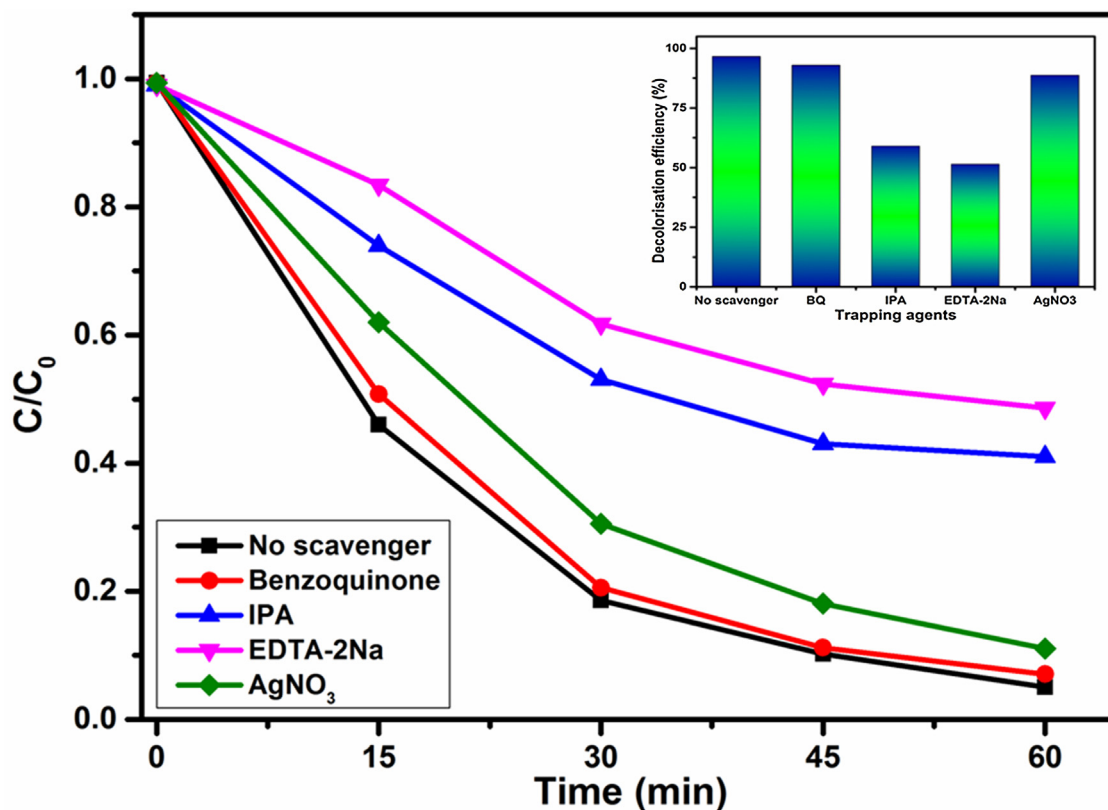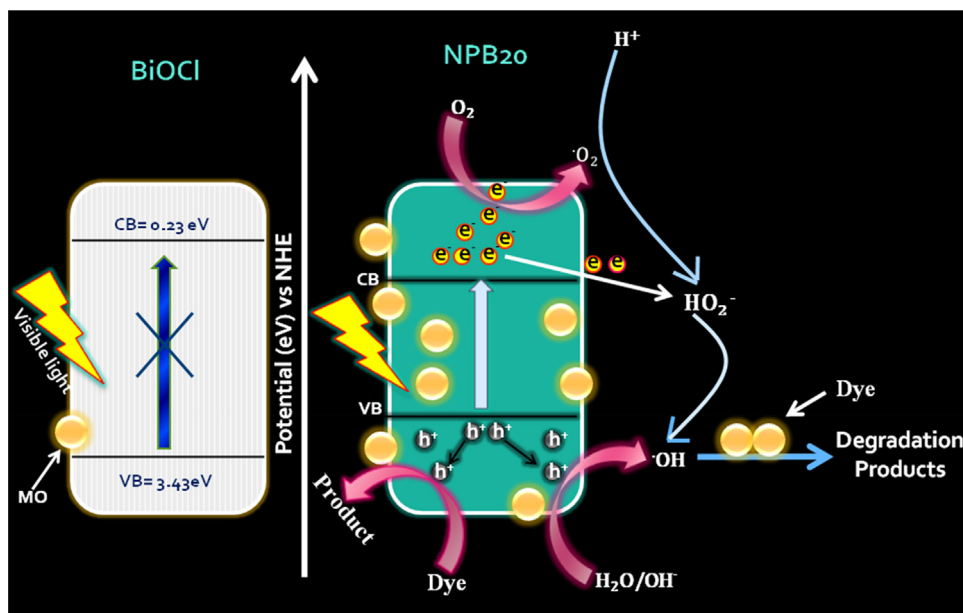
Fig. 13. Effects of various scavengers on the degradation of MO in the presence of NPB20 composite (the dosage of scavengers = 1 mmol L^{-1}) under visible light.

Scheme 2. Possible photodegradation mechanism over NPB20 composite under visible light.

electron-hole pairs in BiOCl, a potential photocatalyst. The results from the PL measurements and active species trapping experiments also conclude that the enhancement in visible light photocatlytic activity of the nanocomposite was mainly attributed to the formation of the heterojunctions between BiOCl and NZF@P and the separation efficiency of photogenerated electron hole pairs. The acquired results from the PXRD, FTIR, SEM, TEM, HRTEM, XPS, EDX, PL, BET and DRS provide that the incorporation of NZF@P nanofibers in layered ternary oxide semiconductor BiOCl improved the porous structure, specific surface area and adsorption property of the composites and offered commendable photocatalytic performance. In anticipation, the finding illustrates the new insight into the photo-
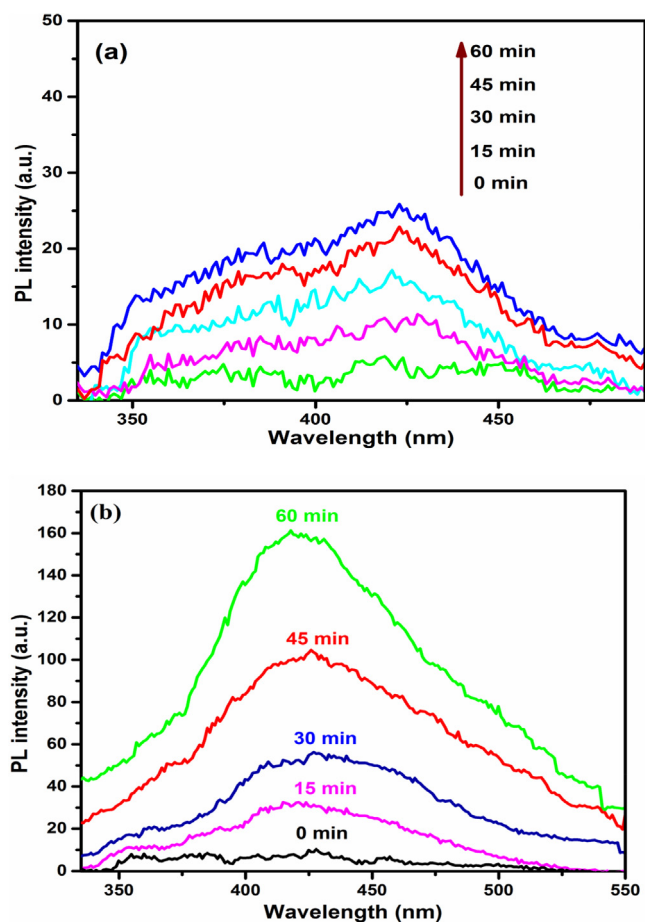
(a)

(b)

Fig. 14. Fluorescence spectral changes observed during illumination of (a) BiOCl and (b) NPB20 composite in terephthalic acid solution. Each fluorescence spectrum was recorded every 15 min of visible light irradiation.
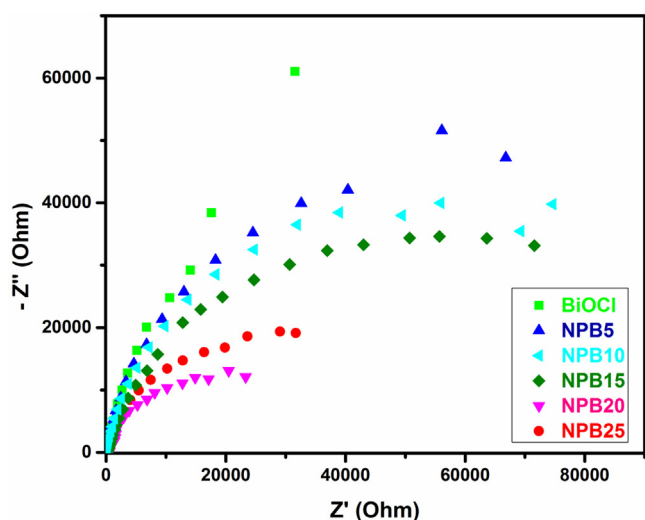

Fig. 15. EIS spectra of BiOCl and NPB composites.
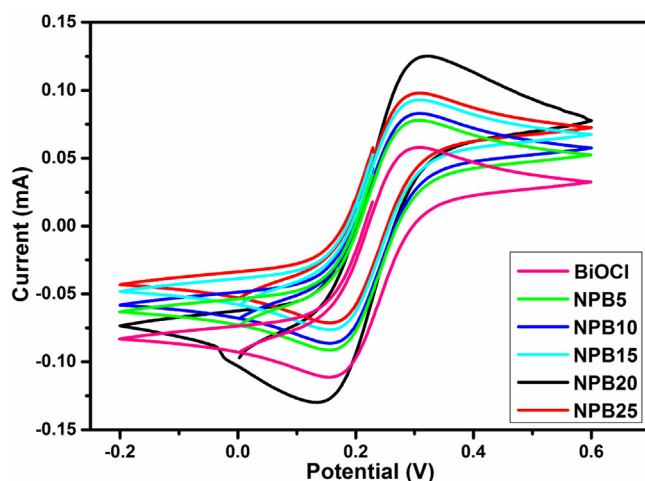
Fig. 16. CV analysis of BiOCl and NPB composites at 5 mV/s scan rate.

Acknowledgment

References

[1] I.C. Pearce, R.J. Lloyd, T.J. Guthrie, Dyes Pigm. 58 (2003) 179–196.
[2] G. Mcmullan, C. Meehan, A. Conneely, N. Kirby, T. Robinson, P. Nigam, M.I. Banat, R. Marchant, F.W. Smyth, Appl. Microbiol. Biotechnol. 56 (2001) 81–87.
[3] M.M. Ayad, A.A. El-Nasr, J. Phys. Chem. C 114 (2010) 612–617.
[4] S.H. Lina, R.S. Juang, Y.H. Wang, J. Hazard. Mater. 113 (2004) 195–200.
[5] C. Neil, R.F. Hawkes, L.D. Hawkes, D.N. Lourenco, N.D. Pinherio, H.M. Dele, J. Chem. Technol. Biotechnol. 74 (1999) 1009–1018.
[6] N.C.T. Martinsa, J. Angelona, A.V. Giraob, T. Trindade, L. Andrad, A. Mendes, Appl. Catal. B: Environ. 193 (2016) 67–74.
[7] A. Fujishima, K. Honda, Nature 238 (1972) 37–45.
[8] J. Hou, C. Yang, Z. Wang, W. Zhou, S. Jiao, H. Zhu, Appl. Catal. B: Environ. 142–143 (2013) 504–511.
[9] H. An, Y. Du, T. Wang, C. Wang, W. Hao, J. Zhang, H. An, Y. Du, T. Wang, C. Wang, W. Hao, J. Zhang, Rare Met. 27 (2008) 243–250.
[10] Z. Deng, D. Chen, B. Peng, F. Tang, Cryst. Growth Des. 8 (2008) 2995–3003.
[11] A.K. Chakraborty, S.B. Rawal, S.Y. Han, S.Y. Chai, W.I. Lee, Appl. Catal. A 407 (2011) 217–223.
[12] F. Chen, H. Liu, S. Bagwasi, X. Shen, J. Zhang, J. Photochem. Photobiol. A: Chem. 215 (2010) 76–80.
[13] M. Nussbaum, N. Shaham-Waldmann, Y. Paz, J. Photochem. Photobiol. A: Chem. 290 (2014) 11–21.
[14] F. Gao, D. Zeng, Q. Huang, S. Tian, C. Xie, Phys. Chem. Phys. 14 (2012) 10572–10578.
[15] Y. Xiang, H. Wang, Y. He, G. Song, Desalin. Water Treat. 55 (2015) 1018–1025.
[16] S.D. Sharma, K.K. Saini, C.P. Sharma, S.C. Jain, Appl. Catal. B: Environ. 84 (2008) 233–240.
[17] T.B. Li, G. Chen, C. Zhou, Z.Y. Shen, R.C. Jin, J.X. Sun, Dalton Trans. 40 (2011) 6751–6758.
[18] S.Y. Chai, Y.J. Kin, M.H. Jung, A.K. Chakraborty, D. Jung, W.I. Lee, J. Catal. 262 (2009) 144–149.
[19] F. Deng, J.L. Min, X. Luo, L.S. Wu, L.S. Luo, Nanoscale 5 (2013) 8703–8710.
[20] M.N. Dimitrijevic, S. Tepavcevic, Z.Y. Liu, T. Tajh, C.S. Silver, M.D. Tiede, J. Phys. Chem. C 117 (2013) 15540–15544.
[21] J. Zhang, R.S. Wang, J.M. Xu, Y. Wang, J.H. Xia, M.S. Zhang, Z.X. Guo, H.S. Wu, J. Phys. Chem. C 113 (2009) 1662–1665.
[22] M.Y. Lin, Z.D. Li, H.J. Hu, C.G. Xiao, X.J. Wang, J.W. Li, Z.X. Fu, J. Phys. Chem. C 116 (2012) (2012) 5764–5772.
[23] M. Radoičicí, Z. Šaponjicí, A.I. Jankovicí, G.C. Marjanovicí, P.S. Ahrenkielc, I.M. Čomor, Appl. Catal. B–Environ. 136 (2013) 133–139.
[24] Q.Z. Yu, M. Wang, H.Z. Chen, Z.W. Dai, Mater. Chem. Phys. 129 (2011) 666–672.
[25] Q. Wang, J. Hu, J. Li, Y. Cai, S. Yin, F. Wang, B. Su, Appl. Surf. Sci. 283 (2013) 577–583.
[26] J.H. Wei, Q. Zhang, Y. Liu, R. Xiong, C.X. Pan, J. Shi, J. Nanopart. Res. 13 (2011) 3157–3165.
[27] H. Zhang, Y.F. Zhu, J. Phys. Chem. C 114 (2010) 5822–5826.
[28] A. Sutka, M. Millers, M. Vanags, U. Joost, M. Maiorov, V. Kisand, R. Pärna, I. Juhnevica, Res. Chem. Intermed. 41 (2015) 9439–9449.
[29] X. Chen, Y. Dai, J. Guo, T. Liu, X. Wang, Ind. Eng. Chem. Res. 55 (2012) 568–578.
[30] E. Casbeer, V.K. Sharma, X.Z. Li, Sep. Purif. Technol. 87 (2012) 01–14.

catalytic domain to engineer a smart modified heterostruted hybrid photocatalyst and bears broad potential applications in the field of water remediation.

[31] I.Y. Choi, I.Y. Kim, W.D. Cho, S.J. Kang, T.K. Leung, Y. Sohn, RSC Adv. 5 (2015) 79624–79634.
[32] Y.H. Zhu, R. Jiang, Q.Y. Fu, R.R. Li, J. Yao, T.S. Jiang, Appl. Surf. Sci. 369 (2016) 01–10.
[33] J.C. Li, N.J. Wang, B. Wang, R.J. Gong, Z. Lin, Mater. Res. Bull. 47 (2012) 333–337.
[34] T. Xie, L. Xu, C. Liu, J. Yang, M. Wang, Dalton Trans. 43 (2014) 2211–2220.
[35] L. Kong, Z. Jiang, T. Xiao, L. Lu, M. Jones, P. Edwards, Chem. Commun. 47 (2011) 5512–5514.
[36] S. Kumar, V. Singh, S. Aggarwal, U.K. Mandal, R.K. Kotnala, J. Phys. Chem. C 114 (2010) 6272–6280.
[37] S. Kumar, V. Singh, S. Aggarwal, U.K. Mandal, R.K. Kotnala, Comp. Sci. Technol. 70 (2010) 249–254.
[38] C. Leng, J. Wei, Z. Liu, R. Xiong, C. Pan, J. Shi, J. Nanopart. Res. 15 (2013) 1643–1654.
[39] F. Liu, Y. Xie, C. Yu, X. Liu, Y. Dai, L. Liu, Y. Ling, RSC Adv. 5 (2015) 24056–24063.
[40] M. Stoyanova, I. Slavova, S. Christoskova, V. Ivanova, Appl. Catal. A: Gen. 476 (2014) 121–132.
[41] A. Rahy, M. Sakrout, S. Manohar, S.J. Cho, J. Ferraris, D.J. Yang, Chem. Mater. 20 (2008) 4808–4814.
[42] R. Tanwar, S. Kumar, U.K. Mandal, J. Photochem. Photobiol. A: Chem. 333 (2017) 105–116.
[43] C. Zeng, Y. Hu, Y. Guo, T. Zhang, F. Dong, Y. Zhang, H. Huang, ACS Sustainable Chem. Eng. 4 (2016) 3305–3315.
[44] J. Yu, W. Wang, B. Cheng, B. Su, J. Phys. Chem. C 113 (2009) 6743–6750.
[45] S. Kumar, V. Singh, S. Aggarwal, U.K. Mandal, Colloid Polym. Sci. 287 (009) (2017) 1107–1110.
[46] B. Pare, B. Sarwan, S.B. Jonnalagadda, Appl. Surf. Sci. 258 (2011) 247–253.
[47] H. Gnayem, Y. Sasson, J. Phys. Chem. C 119 (2015) 19201–19209.
[48] J. Xia, L. Xu, J. Zhang, S. Yin, H. Li, H. Xu, J. Dia, CrystEngComm 15 (2013) 10132–10141.
[49] S.H. Piao, M. Bhaumik, A. Maity, H.J. Choi, J. Mater. Chem. C 3 (2015) 1861–1868.
[50] Ta-I. Yang, R.N.C. Brown, L.C. Kempel, P. Kofinas, J. Nanopart. Res. 12 (2010) 2967–2978.
[51] M. Guerrero, A. Altube, E. Garcia-Lecina, E. Rossinyol, M.D. Baro, E. Pellicer, J. Sort, ACS Appl. Mater. Inter. 6 (2014) 13994–14000.
[52] J. Yu, J. Low, W. Xiao, P. Zhou, M. Jaroniec, J. Am. Chem. Soc. 25 (2014) 8839–8842.
[53] J. Di, X.J. Xia, S. Yin, H. Xu, L. Xu, G.Y. Xu, Q.M. He, M.H. Li, RSC Adv. 4 (2014) 14281–14290.
[54] Y.H. Zheng, C.Q. Chen, Y.Y. Zhan, X.Y. Lin, Q. Zheng, K.M. Wei, J.F. Zhu, Inorg. Chem. 46 (2007) 6675–6682.
[55] S. Min, F. Wang, Y. Han, J. Mater. Sci. 42 (2007) 9966–9972.
[56] F. Wang, S.X. Min, Chin. Chem. Lett. 18 (2007) 1273–1277.
[57] A.P. Finlayson, V.N. Tsaneva, L. Lyons, M. Clark, B.A. Glowacki, Phys. Stat. Solid A 203 (2006) 327–335.
[58] Z. Liu, X. Xu, J. Fang, X. Zhu, B. Li, Water Air Soil Pollut. 5 (2012) 2783–2798.
[59] L. Ye, J. Liu, C. Gong, L. Tian, T. Peng, L. Zan, ACS Catal. 2 (2012) 1677–1683.
[60] Y. Lin, D. Li, J. Hu, G. Xiao, J. Wang, W. Li, X. Fu, Phys. Chem. C 116 (2012) 5764–5772.
[61] T. Xu, Y. Cai, K.K. O'Shea, Environ. Sci. Technol. 41 (2007) 5471–5477.
[62] Y. Shi, Z. Yang, Y. Liu, J. Yu, F. Wang, J. Tong, B. Sua, Q. Wang, RSC Adv. 6 (2016) 39774–39783.
[63] Y.W. Teoh, A.J. Scott, R. Amal, J. Phys. Chem. Lett. 3 (2012) 629–639.
[64] P. Salvador, J. Phys. Chem. C 111 (2007) 17038–17043.
[65] S. Khanchandani, S. Kumar, A.K. Ganguli, ACS Sustain. Chem. Eng. 4 (2016) 1487–1499.
[66] X. Pan, L. Wang, X. Sun, B. Xu, X. Wang, Ind. Eng. Chem. Res. 30 (2013) 10105–10113.
[67] M.G. Leelavathi, N. Ravishankar, J. Am. Chem. Soc. 41 (2014) 14445–14455.
[68] X. Gao, X. Liu, Z. Zhu, X. Wang, Z. Xie, Sci. Rep. 6 (2016).
[69] G. Nie, X. Lu, W. Wang, M. Chi, Y. Jianga, C. Wang, Mater. Chem. Front. (2016), http://dx.doi.org/10.1039/c6qm00232c.
[70] N. Gua, Y. Liang, S. Lan, L. Liu, J. Zhang, G. Ji, S. Gan, J. Phys. Chem. C 118 (2014) 18343–18355.
[71] H. Zhang, R.L. Zong, J.C. Zhao, Y.F. Zhu, Environ. Sci. Technol. 42 (2008) 3803–3807.
[72] T. Tangcharoen, A. Ruangphanit, W. Klyubun, W. Pecharapa, J. Sol-Gel. Sci. Technol. 66 (2013) 387–398.
[73] L. Sun, L. Xiang, X. Zhao, C.-J. Jia, J. Yang, Z. Jin, X. Cheng, W. Fan, ACS Catal. 5 (2015) 3540–3551.